JCTC Journal of Chemical Theory and Computation

Article

pubs.acs.org/JCTC

Different Ways of Hydrogen Bonding in Water - Why Does Warm Water Freeze Faster than Cold Water?

Yunwen Tao,[†] Wenli Zou,[†] Junteng Jia,[‡] Wei Li,[‡] and Dieter Cremer*[,†]

[†]Computational and Theoretical Chemistry Group (CATCO), Department of Chemistry, Southern Methodist University, 3215 Daniel Avenue, Dallas, Texas 75275-0314, United States

[‡]Institute of Theoretical and Computational Chemistry, Key Laboratory of Mesoscopic Chemistry of MOE, School of Chemistry and Chemical Engineering, Nanjing University, Nanjing 210023, P. R. China

Supporting Information

ABSTRACT: The properties of liquid water are intimately related to the H-bond network among the individual water molecules. Utilizing vibrational spectroscopy and modeling water with DFT-optimized water clusters (6-mers and 50-mers), 16 out of a possible 36 different types of H-bonds are identified and ordered according to their intrinsic strength. The strongest H-bonds are obtained as a result of a concerted push−pull effect of four peripheral water molecules, which polarize the electron density in a way that supports charge transfer and partial covalent character of the targeted H-bond. For water molecules with tetra- and pentacoordinated O atoms, H-bonding is often associated with a geometrically unfavorable positioning of the acceptor lone pair and donor $\sigma^*(OH)$ orbitals so that electrostatic rather than covalent interactions increasingly dominate H-bonding. There is a striking linear dependence between the intrinsic strength of H-bonding as measured by the local H-bond stretching force constant and the delocalization energy associated with charge transfer. Molecular dynamics simulations for 1000-mers reveal that with increasing temperature weak, preferentially electrostatic H-bonds are broken, whereas the number of strong H-bonds increases. An explanation for the question why warm water freezes faster than cold water is given on a molecular basis.

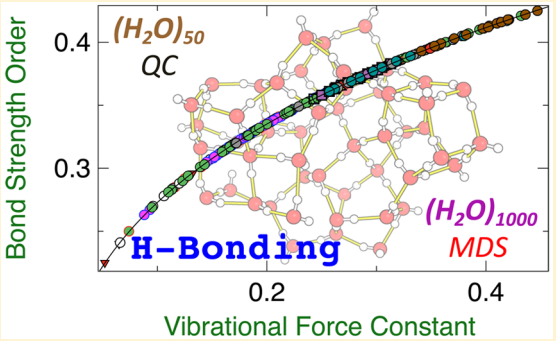

INTRODUCTION

The understanding of hydrogen bonding (H-bonding) is essential for unravelling many biological and environmental phenomena.[1−6] H-bonding dominates the noncovalent interactions between the molecules in liquid water, and in this way H-bonding is ultimately responsible for the unique properties of water. Essential for the understanding of the complex structure and dynamics of liquid water[7] is the study of H-bonding with the help of quantum chemical methods. If an atomistic approach is used, liquid water can be modeled by using clusters of water molecules. The smallest of such clusters, the water dimer, is only used for reference purposes, and its properties in connection with H-bonding are fairly well-known.[8−20] Also, larger clusters with three to six water molecules have been reliably described and have helped to extend the understanding of H-bonding between water molecules.[21−36] Less frequent are high-accuracy investigations of larger water clusters.[37] Most of these investigations have been carried out at the Hartree−Fock (HF), Density Functional Theory (DFT), or perturbation theory level. For example, the investigation of 20-mers (clusters with 20 water molecules),[38−41] 25-mers,[42] 30-mers up to 40-mers,[43−49] or even 60-mers has to be reported.[50]

Noteworthy in this connection is that the vibrational spectra of 20-mers have been investigated in detail by Xantheas and co-workers using second order perturbation theory.[38] DFT benchmark calculations utilizing B3LYP, X3LYP, and M06-type of XC-functionals for predicting binding energies of water clusters up to 20 molecules have been carried out by Bryantsev and co-workers.[39] Parthasarathi and co-workers found that linear chains of up to 20 water molecules lead to dipole moments as high as 41 D thus emphasizing the cooperative effect of H-bonding in larger clusters.[40] An interesting study on the polarizability of water clusters and the charge flow through H-bonds in the presence of internal and external electric fields was carried out by Yang and co-workers.[41] The electron density at the critical points of the H-bonds of a water cluster was analyzed by Neela and co-workers who predicted an increase of the density with the cluster size.[51] Iwata pointed out the importance of charge transfer and dispersion energies in $(H_2O)_{20}$ and $(H_2O)_{25}$, which he found to depend on the O···O distance.[42] Lenz and co-workers[43] calculated the vibrational spectra of water clusters containing up to 30 water molecules. They found a correlation between the red-shift of the O−H donor stretching frequency and the type of H-bond based on the coordination numbers of the O atoms being involved. The importance of the collective electrostatic effects on H-bonding

Received: July 23, 2016
Published: December 6, 2016

DOI: 10.1021/acs.jctc.6b00735
J. Chem. Theory Comput. 2017, 13, 55−76

as caused by the nonimmediate environment in liquid water models was emphasized by Bako and co-workers.[44] Qian and co-workers did systematic studies on water clusters of different size ranging from the dimer to 34-mers using HF/6-31G(d).[47] An attempt was made by Huang and co-workers to predict the far-infrared spectra of water clusters up to 38 molecules with DFT and to relate them to observed THz spectra.[48] Specific forms of water clusters were investigated by various authors (spiro-cyclic,[45] fullerene-shaped[50]). Frogato and co-workers performed ab initio Born−Oppenheimer molecular dynamics (MD) simulations for 69-mer clusters containing an excess electron.[52] Clusters with up to 280 water molecules were investigated by Loboda and co-workers who determined averaged H-bond energies.[53] Turi used mixed quantum-classical MD simulations for a cluster consisting 1,000 water molecules either in neutral state or with an excess electron.[54] A quantum simulation of water was carried out by Wang and co-workers.[55]

In these investigations, the intrinsic strength of the H-bond in water clusters or liquid water could not be determined. Instead one attempted to obtain indirect evidence by analyzing binding energies, H-bond distances, vibrational frequencies, electron densities at the H-bond critical point, and other molecular properties, which can only provide a qualitative measure of the H-bond strength as they relate to all intermolecular forces and interaction energies.

In this work, we present the harmonic vibrational frequencies of water clusters containing 50 molecules (*50-mers*) that can be considered as suitable models for distinguishing between different H-bond types. For the first time, we will provide a detailed account on H-bonding in water clusters, which can be considered as suitable models for liquid water. In connection with this general goal, we pursue the following objectives: (i) We will investigate how many of the 36 possible standard H-bond types (excluding pentacoordination of oxygen and H-bond bifurcation) are needed to analyze H-bonding in the 50-mers. (ii) We will characterize the various H-bonds according to the intrinsic strength of their interactions, which we will characterize with the properties of the H-bond stretching vibrations using the theory of Konkoli and Cremer for analyzing local vibrational modes.[56−59] For this purpose, we will derive a H-bond strength order (BSO) value, which will provide a quantitative measure to compare different H-bonds in the water clusters investigated. (iii) H-bonding results from the noncovalent interactions of a H-bond donor (D) and a H-bond acceptor (A). Accordingly, we will investigate to which extent the properties of D and those of A are varied by H-bonding. Are there relationships between H-bond stretching force constants, covalent and electrostatic bond character, electron and energy density properties at the H-bond critical points, or the H-bond lengths? (iv) Is there a relationship between the strength of the OH donor bond and that of the H-bond, which can be used to characterize the latter via properties of the former?[5,6] (v) Finally, we will make an attempt to relate the structure of a water-cluster to the macroscopic properties of liquid water by utilizing MD simulations of 1000-mers. In this connection, we will investigate the question why warmer water freezes more quickly than colder water.[60−66]

The results of this investigation will be presented in the following order. In Section 2, we will describe the computational methods used in this work. In Section 3, the different H-bonds of the 50-mers will be analyzed, and a suitable way of describing them will be worked out. The results of this analysis will be applied in Section 4 to provide a molecular explanation to the phenomenon that warm water freezes faster than cold water. The chemical relevance and the conclusions of the current investigation will be summarized in the last section.

COMPUTATIONAL METHODS

Equilibrium geometries and normal vibrational modes were calculated using the ωB97X-D density functional,[67,68] which was chosen because it provides a reliable description of noncovalent interactions in cases where dispersion and other long-range van der Waals interactions play an important role.[69−72] Pople's triple-ζ basis 6-311G(d,p) was augmented by diffuse functions for H and O atoms. The 6-311++G(d,p) basis set[73−75] thus obtained contained 1800 basis functions for the 50-mers. The calculations of the normal mode vectors and frequencies were carried out with the GEBF (generalized energy-based fragmentation) method[76,77] at the ωB97X-D/6-311++G(d,p) level. The analytical gradient of the GEBF method[77] was used for the geometry optimization, whereas for the GEBF Hessian an approximate expression was employed.[78] The usefulness of GEBF-ωB97X-D in the case of the water clusters was first tested by carrying out calculations for 20-mers and comparing results obtained with CCSD(T)[79] in the form of GEBF-CCSD(T). GEBF-ωB97X-D turned out to be both reliable and cost efficient.

In the GEBF-ωB97X-D calculations, each water molecule was selected as a fragment, and the distance threshold was set to 4.0 Å, i.e. at least one atom is within this limit. The maximum number of fragments in each subsystem was limited to seven. Natural population analysis (NPA)[80,81] charges were employed as background charges, and two-fragment subsystems with a distance threshold of 8.0 Å were considered for corrections. The DFT calculations were carried out using a pruned (75,302) fine grid[82,83] and tight convergence criteria in the geometry optimizations to guarantee a reliable calculation of vibrational frequencies. The initial geometries of the 50-mers were taken from MD calculations using a TIP4P force field.[84] The optimized geometries are given in the Supporting Information (SI). The relative energies of the complexes used in this investigation are 0.0 kcal/mol (cluster **A**; absolute energy: −3822.655729 hartree), −0.62 (**B**), 10.30 (**C**), and 4.40 kcal/mol (**D**). The lowest vibrational frequencies obtained in this way are 23.7, 26.3 (cluster **A**); 25.2, 29.6 (**B**); 18.0, 21.3 (**C**); 17.9, 23.4 cm^{-1} (**D**). Another water complex leading to an imaginary frequency was excluded from the investigation.

Electron density and energy density distributions were calculated using ωB97X-D rather than GEBF-ωB97X-D. The charge transfer analysis was carried out on the basis of calculated NPA charges.[80,81] A topological analysis of the electron density distribution $\rho(\mathbf{r})$ was performed.[85] The nature of the H-bond was determined by the energy density $H(\mathbf{r})$ calculated at the H-bond critical point $\mathbf{r}_b$ and the application of the Cremer−Kraka criteria for covalent bonding: (i) A zero-flux surface and bond critical point $\mathbf{r}_b$ have to exist between the atoms in question (necessary condition). (ii) The local energy density at $H(\mathbf{r}_b)$ must be negative and thereby stabilizing (sufficient condition for covalent bonding). A positive $H(\mathbf{r}_b)$ indicates a dominance of electrostatic interactions.[86−88] Hence, the Cremer−Kraka criteria can reveal whether H-bonding is covalent, electrostatic, or a mixture of both (values close to zero).

The covalent character of the H-bond was estimated by calculating the delocalization energy $\Delta E(del)$, which is associated with the charge transfer from a lone pair orbital of

DOI: 10.1021/acs.jctc.6b00735
J. Chem. Theory Comput. 2017, 13, 55−76

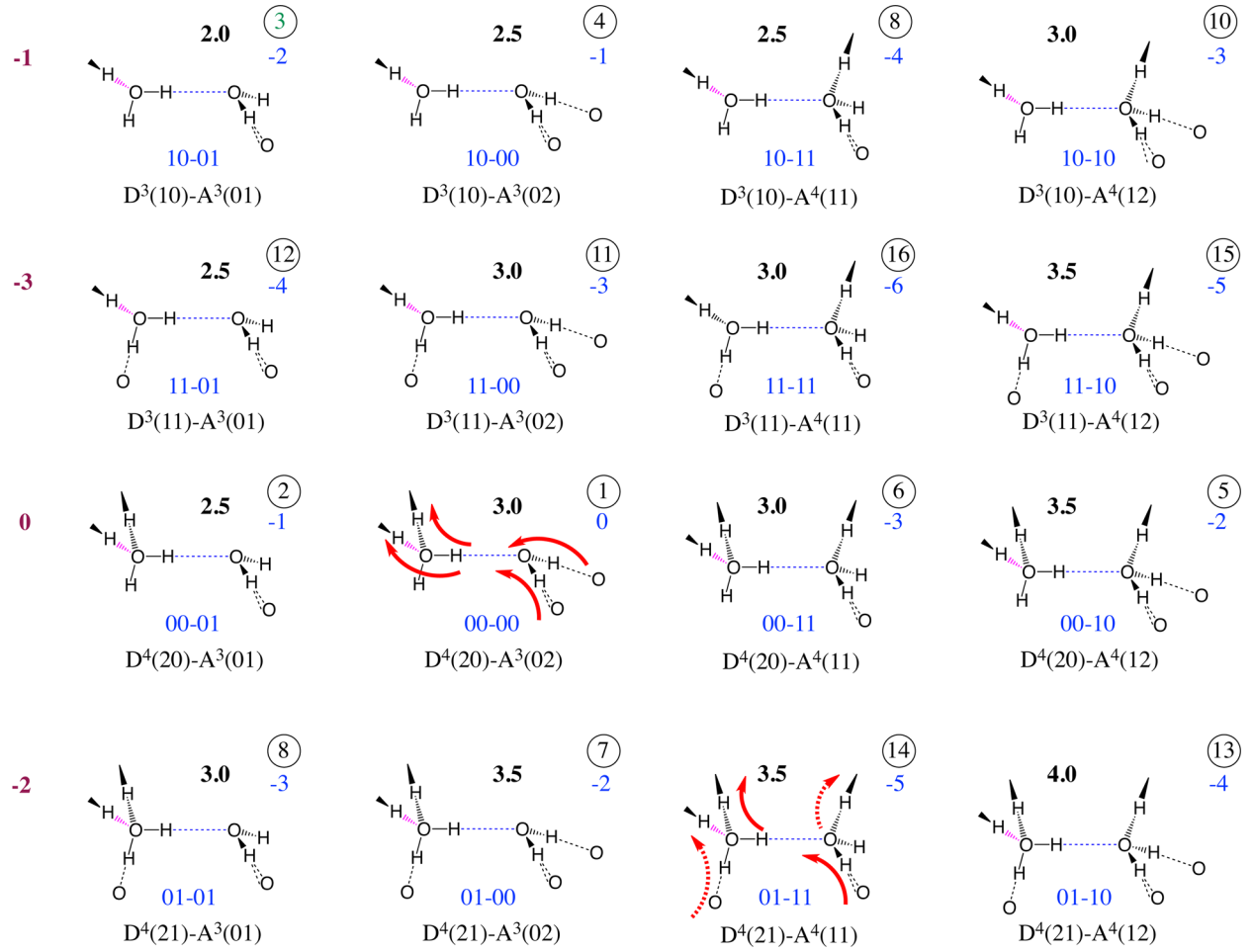

Figure 1. Coding of the 16 H-bond types discussed for the 50-mers by the notation $D^{c_D}(i_a,j_d) - A^{c_A}(k_a,l_d)$. The integers i_a, j_d, k_a, and l_d give the peripheral (external) H-bonds directly embedding the targeted H-bond, i.e. the acceptor (a) and donor (d) H-bonds of D and A, which are ≤2 for the D or A water molecule. The superscripts c_D and c_A are the coordination numbers of O(D) and O(A), respectively, which vary between 3 and 4 and must be distinguished from the number of H-bonds $m(D)$ and $m(A)$. In black bold print the average $m(AD)$ of $m(D)$ and $m(A)$ is given. For the strongest H-bond $D^4(20) - A^3(02)$ (in short: 20-02) red arrows indicate the direction of charge polarization, which supports the covalent character of this H-bond. For other H-bonds, the optimal 20-02 arrangement is perturbed as indicated for the $D^4(21) - A^4(11)$ (in short: 21-11) H-bond by dashed red arrows. For each type of H-bond, the deviation is given in blue as in the case of the 21-12 H-bond: |21-11 - 20-02 | = 01-11. The distortion descriptor (see text) is given as a negative blue number in the upper right of each drawing where an encircled number defines the position of the H-bond in a strength order from 1 (strongest H-bond) to 16 (weakest H-bond) according to the average BSO values of Figure 3. The 10-01 bond value has been added as reference (BSO: n = 0.399; see text). On the left, the distortion relationship between rows of the matrix of H-bond types is given in brown color.

A to an antibonding OH orbital of D thus leading to an increase of the electron density in the range of the H-bond. The magnitude of $\Delta E(del)$ was determined by second order perturbation theory[81] where both $lp(O) \rightarrow \sigma^*(OH)$-contributions to $\Delta E(del)$ for a given $O\cdots OH$-interaction were included (see Section 3).

The intrinsic strength of the H-bond was determined by using the local H-bond stretching force constant.[59,89] The local vibrational modes of Konkoli and Cremer[56] are based on the solution of the Wilson equation of vibrational spectroscopy[90]

$$\mathbf{F}^q\mathbf{D} = \mathbf{G}^{-1}\mathbf{D}\mathbf{\Lambda} \tag{1}$$

in the form[91]

$$(\mathbf{G}_d + \lambda\mathbf{G}_{od})\tilde{\mathbf{R}}_\lambda = (\mathbf{\Gamma}^q_d + \lambda\mathbf{\Gamma}^q_{od})\tilde{\mathbf{R}}_\lambda\mathbf{\Lambda}_\lambda \tag{2}$$

In these two equations, $\mathbf{F}^q$ is the calculated force constant matrix expressed in internal coordinates q_n, $\mathbf{D}$ collects the corresponding vibrational eigenvectors $\mathbf{d}_\mu$ as column vectors (μ = 1, ⋯, N_{vib} with $N_{vib} = 3N - L$, N: number of atoms; L: number of translations and rotations), $\mathbf{G}$ is the Wilson matrix for the kinetic energy,[90] and $\mathbf{\Lambda}$ is a diagonal matrix containing the vibrational eigenvalues $\lambda_\mu = 4\pi^2c^2\omega_\mu^2$. In the expression for the eigenvalues, ω_μ represents the vibrational frequency of mode $\mathbf{d}_\mu$.

Matrix $\mathbf{\Gamma}$ in eq 2 is the inverse force constant matrix, which is usually called compliance matrix.[92] Matrix $\tilde{\mathbf{R}}$ corresponds to $\tilde{\mathbf{D}}$ in the local mass-weighted formulation (indicated by the tilde)[91]

$$\tilde{\mathbf{R}} = \mathbf{F}^q\tilde{\mathbf{D}} \tag{3}$$

and the partitioning is into diagonal (d) and off-diagonal (od) parts. The parameter λ controls kinematic (mass) coupling, i.e. for λ = 0 the local description is obtained and for λ = 1 the Wilson equation reformulated in terms of compliance matrix and $\mathbf{R}$ modes.

Solution of the Wilson equation requires the diagonalization of matrix $\mathbf{F}^q$ to give the matrix $\mathbf{K}$. In this way, the electronic

DOI: 10.1021/acs.jctc.6b00735
J. Chem. Theory Comput. 2017, 13, 55−76

coupling between the local modes is eliminated. Solving the mass-decoupled Wilson equation leads to the mass-decoupled local modes $\mathbf{a}_n$,[91] which can be written as[56,58,93]

$$\mathbf{a}_n = \frac{\mathbf{K}^{-1}\mathbf{d}_n^{\dagger}}{\mathbf{d}_n\mathbf{K}^{-1}\mathbf{d}_n^{\dagger}} \tag{4}$$

where $\mathbf{d}_n$ is now a row vector of matrix $\mathbf{D}$. The local mode force constant k_n^a is given by eq 5

$$k_n^a = \mathbf{a}_n^{\dagger}\mathrm{K}\mathrm{a}_n \tag{5}$$

and the local mode frequency ω_n^a can be obtained from

$$(\omega_n^a)^2 = \frac{G_{nn}k_n^a}{4\pi^2c^2} \tag{6}$$

where element G_{nn} of matrix $\mathbf{G}$ defines the local mode mass.[56]

Before continuing it is useful to point out that the term *local vibrational modes* is sometimes used in a different context: Henry and co-workers[94−96] use the term in connection with the (an)harmonic oscillator models to quantum mechanically calculate the overtones of XH stretching modes. The higher overtone modes (n = 5 or 6) for isolated XH groups are largely decoupled which justifies using the term local modes. Their frequencies correlate linearly with the Konkoli−Cremer local mode frequencies thus verifying their local mode character;[97] however, they are only accessible for a few types of XH stretching modes, whereas the Konkoli−Cremer modes are generally defined and will be exclusively used in the following.

The relative bond strength order (BSO) n of an OH bond is obtained by utilizing the extended Badger rule,[97−99] according to which the BSO is related to the local stretching force constant k_a by a power relationship, which is fully determined by two reference values and the requirement that for a zero-force constant the BSO value becomes zero. Accordingly, the relationship $n(OH) = a(k_a)^b$ can be derived from two suitable reference bonds. In this work, the constants a and b were determined for FH bonds using the frequencies of F−H (n = 1) and the $D_{\infty h}$-symmetrical $[F\cdots H\cdots F]^-$ anion (n = 0.5) as suitable references. Since the Badger and extended Badger rules predict for related XH bonds the same power relationship, the equation $n(FH) = a(k_a)^b$ with a = 0.5402 and b = 0.2966 was also used for the OH bonds after shifting the single bond reference (corresponding to a n(OH) = 0.9653) by 0.0347 so that the OH bonds of H_2O obtain the BSO value n = 1.00.

In the MD simulations, 1000 water molecules in a PBC (periodic boundary condition) box were simulated by classical MD using the TIP5P[100] force field in the NPT ensemble at 1.0 bar and 283, 308, 363, and 378 K where the simulations at 308 and 378 K were used as control calculations and therefore will not be discussed here in detail. The cutoff of nonbonded interactions was set to be 8 Å, and the Coulombic interactions were treated with the Ewald summation.[101] The temperature was scaled by Langevin dynamics with the collision frequency γ being 1.0.[102] The Berendsen bath coupling method[103] was selected as a thermostat algorithm to control the pressure. The equations of the motion were integrated by the velocity Verlet algorithm[104] with OH bond constrains.[105,106] The time step was set to 1 fs (femtosecond), and the trajectories were collected for every 100 fs. The simulation time was 2 ns (nanoseconds) where the first ns was used for reaching the equilibrium. The trajectories of the second ns were used for the analysis. From the snapshots of the second ns, 1000 $(H_2O)_{1000}$ periodic clusters were taken out using equal time intervals of 1 ps (picosecond).

For the analyses, a H-bond was considered to be given if the H···O distance is between 1.5 and 2.2 Å, and the O−H···O angle is larger than 100.0°. PBC were also employed for determining H-bonds. In the analysis of the $(H_2O)_{50}$ clusters, the 2.2 Å limit turned out to be a reasonable cutoff value. There are 6 × 6 = 36 standard H-bond types (excluding bifurcated H-bonds and pentacoordination at the O atom, i.e. the maximum number of H-bonds per water molecule is limited to 4). If pentacoordination is included another 36 types of H-bonds are possible, whereas bifurcation adds another 71 H-bond types (maximum number of H-bonds ≤5) thus leading to a total of 11 × 13 = 143 different H-bond types. For the bifurcated H-bonds, the H atom of the O−H donor bond is within 2.4 Å with regard to two neighboring O atoms.[107] In the equilibrium structures of the 50-mers, only a fraction of the maximally possible standard H-bonds can occur. These are shown in Figure 1 where the H-bond of the cyclic water hexamer, $(H_2O)_6$, is used as a suitable reference (see the SI for the equilibrium geometry). The average number of H-bonds per water molecule was obtained by the formula $m_{av} = 2 \times N(H\ bonds)/N(water\ molecules)$ (N: number). In addition, we use the quantities $m(D)$ and $m(A)$, which give the total number of H-bonds of the D- and the A-water for a given type of H-bond (Figure 1). Accordingly, the average $m(AD)$ is equal to $[m(D) + m(A)]/2$. Similarly, the number of peripheral H-bonds can be given by $m_p(D)$, $m_p(A)$, etc. Parameters m and m_p are associated with the dimer D−A and do not consider peripheral H_2O molecules (m_{av} varies only slightly from 1.5 to 1.75 for the cases considered and therefore is less useful for the characterization of the types of H-bonds shown in Figure 1).

Beside calculating the charge transfer between the interacting monomers using NPA values, we also calculated the difference density distribution $\Delta\rho(\mathbf{r}) = \rho(Complex,\mathbf{r}) - \rho(Monomer1,\mathbf{r}) - \rho(Monomer2,\mathbf{r})$, which was determined and plotted for the complex-enveloping surface of an electron density distribution of 0.001 e/Bohr^3. For the situation of six water molecules as in 20-02 (see below), the geometry was taken from one of the 20-02 H-bonds of cluster **A**. The polarization effect caused by the four peripheral H_2O was determined by subtracting from the hexamer density that of the trimers on the D and A side as well as that of the central D−A dimer and then adding the density of the D and A water monomer (short notation: 6-2 × 3-2 + 1 + 1) all calculated in the geometry of the hexamer. In this way, the density contributions of the trimers and the difference density of the central dimer were eliminated so that the *push−pull* effect of the peripheral water molecules on the central dimer unit becomes visible.

For the statistical analysis, we used box-and-whisker diagrams,[108] which present the distribution of data by a box and two whiskers. Minimum and maximum values are indicated by two horizontal lines. The first and third quartile of data, Q1 and Q3, define the bottom and top of the box where Q2 gives the position of the median. The interquartile range QR = Q3 − Q1 gives the vertical length of the box. The length of the whiskers is defined by Q1 − 1.5 QR (lower whisker) and Q3 + 1.5 QR (upper whisker). Any data point, which is lower than $Q1 - q \times QR$ and higher than $Q3 + q \times QR$, is considered a mild outlier for q = 1.5 (black dots) and an extreme outlier for q = 3.0 (open dots).[108] We have applied this analysis when at least more than 7 data points were available.

DOI: 10.1021/acs.jctc.6b00735
J. Chem. Theory Comput. 2017, 13, 55−76

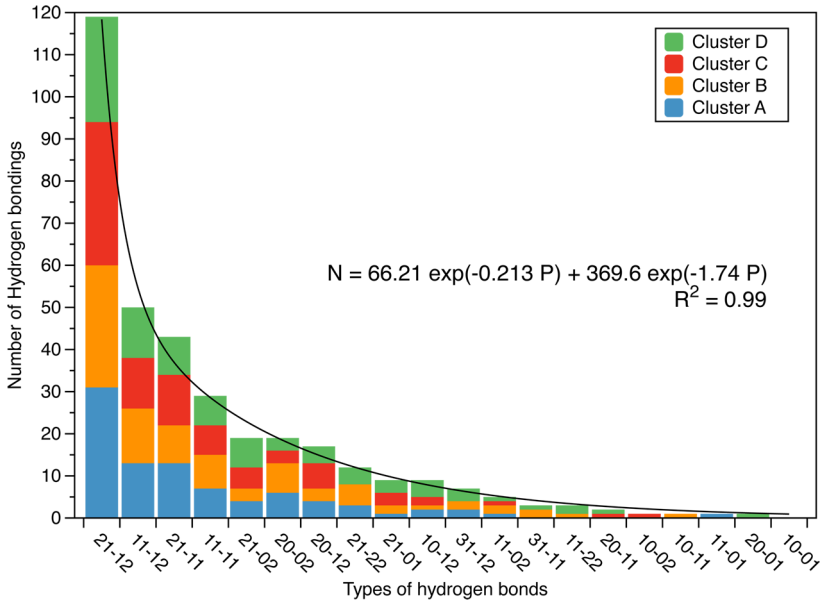

Figure 2. Distribution of different H-bonds in the four 50-mers **A** (blue), **B** (orange), **C** (red), and **D** (green). The H-bonds are classified according to Figure 1 and ordered according to their frequency of appearance, which can be approximately described by an exponential dependence of the number N of H-bonds (P: position number). See text.

All vibrational mode and electron density calculations were carried out with the program package COLOGNE2016,[109] whereas for the DFT and the GEBF calculations local versions of the program package Gaussian09[110] were used. All MD simulations were performed with the AmberTools15 package.[111] Difference densities were plotted with the program Multiwfn.[112]

THE H-BONDING NETWORK IN WATER CLUSTERS

The H-bond between a D- and an A-molecule can be characterized by the notation $D^{c_D}(i_a,j_d)-A^{c_A}(k_a,l_d)$ where integers i_a, j_d, k_a, and l_d give the peripheral (external) H-bonds directly embedding the targeted H-bond, i.e. the acceptor (a) and donor (d) H-bonds of D and A, which for the D or A water molecule are normally equal to or smaller than 2. The superscripts c_D and c_A are the coordination numbers of O(D) and O(A), respectively, which vary between 3 and 4 in the case of the 50-mers. Hence, $D^4(20) - A^3(02)$ (or in short (20-02)) denotes the H-bond with a D water molecule functioning as an acceptor for 2 external (=peripheral) H-bonds (its O atom coordinates with 4 H via normal or H-bonding; c_D = 4) and an A water molecule that itself is functioning as a double donor for 2 other external H-bonds (c_A = 3). This situation is sketched in the third row, second column of Figure 1. In the equilibrium geometry of the 50-mers, each D-molecule and each A-molecule are found to undergo one of the four possible interactions: 1) 10; 2) 11; 3) 20; 4) 21, which leads to a total of 16 = 4^2 different H-bond interactions such as 10-01, 10-02, 10-11, 10-12, ··· 21-12, where we have used as a reference the relatively strong 10-01 H-bond of cyclic $(H_2O)_6$. The largest number of peripheral H-bonds is realized for the H-bond $D^4(21) - A^4(12)$, which has for both the D and A molecule 2 + 2 = 4 H-bonds and by this $(i_a + j_d) + (k_a + l_d)$ = 3 + 3 = 6 peripheral H-bonds influencing the targeted D−A H-bond. Figure 1 contains additional information, which will be discussed below. In passing, we note that in liquid water, contrary to the equilibrium situation of a 50-mer, other relative weak H-bonds or no H-bonds at D and/or A are observed so that for each water molecule 6 rather than 4 different H-bond arrangements become possible leading to a total of 6^2 = 36 H-bond types (see Figure S1 in the SI). The complete set of H-bond types will be discussed in Section 4. Finally, it has to be mentioned that similar notations on how to characterize different types of H-bonding in water clusters have been used in the literature (see Figure S1 of the SI for a relationship between these and the current notation).[42,113−115]

The numbering of atoms for the almost spherical structures of the four 50-mers is given in Figures S2−S5 of the SI. It is obvious that the water molecules located at the outside of the sphere have a smaller number of H-bonds than those water molecules positioned closer to the center of the 50-mer. In the four 50-mers **A**, **B**, **C**, and **D**, a total of 350 H-bonds (87,88,88,87) are found, which account for 15 of the 16 types of H-bonds shown in Figure 1. The 10-01 H-bond is topologically only possible in isolated cyclic water clusters as in $(H_2O)_6$ that we have used as a reference. In addition to the H-bond types of Figure 1, there are 20 H-bonds which were not found for the 50-mers but will be discussed in connection with the MD simulations. In Table S1 of the SI, all H-bonds identified for clusters **A**, **B**, **C**, and **D** are characterized by the $R(H\cdots O)$ distance, the local stretching force constant $k^a(H\cdots O)$, the associated local stretching frequency $\omega^a(H\cdots O)$, the BSO value $n(H\cdots O)$, and the $O-H\cdots O$ angle α.

As one can see from the H-bond data (Table S1 in the SI, Figure 2), different types of H-bonding differ significantly in their number, where however their distribution is similar in the four water clusters. The distribution of the various types of H-bonding is nearly the same in the four 50-mers, which might be a result of their spherical form. The average number of H-bonds per water molecule, m_{av}, is close to 3.5 in all cases (Table S1 in the SI).

The most common H-bond is that of the 21-12 type (number of peripheral H-bonds: $m_p(D)$ = 3; $m_p(A)$ = 3; in short (3,3)), which accounts for 34.0% of all H-bonds followed by 11-12 ((2, 3); 14.3%), 21-11 ((3,2), 12.3%), and 11-11 H-bond ((2,2), 8.3%). The H-bond 11-02 is the least common

DOI: 10.1021/acs.jctc.6b00735
J. Chem. Theory Comput. 2017, 13, 55−76

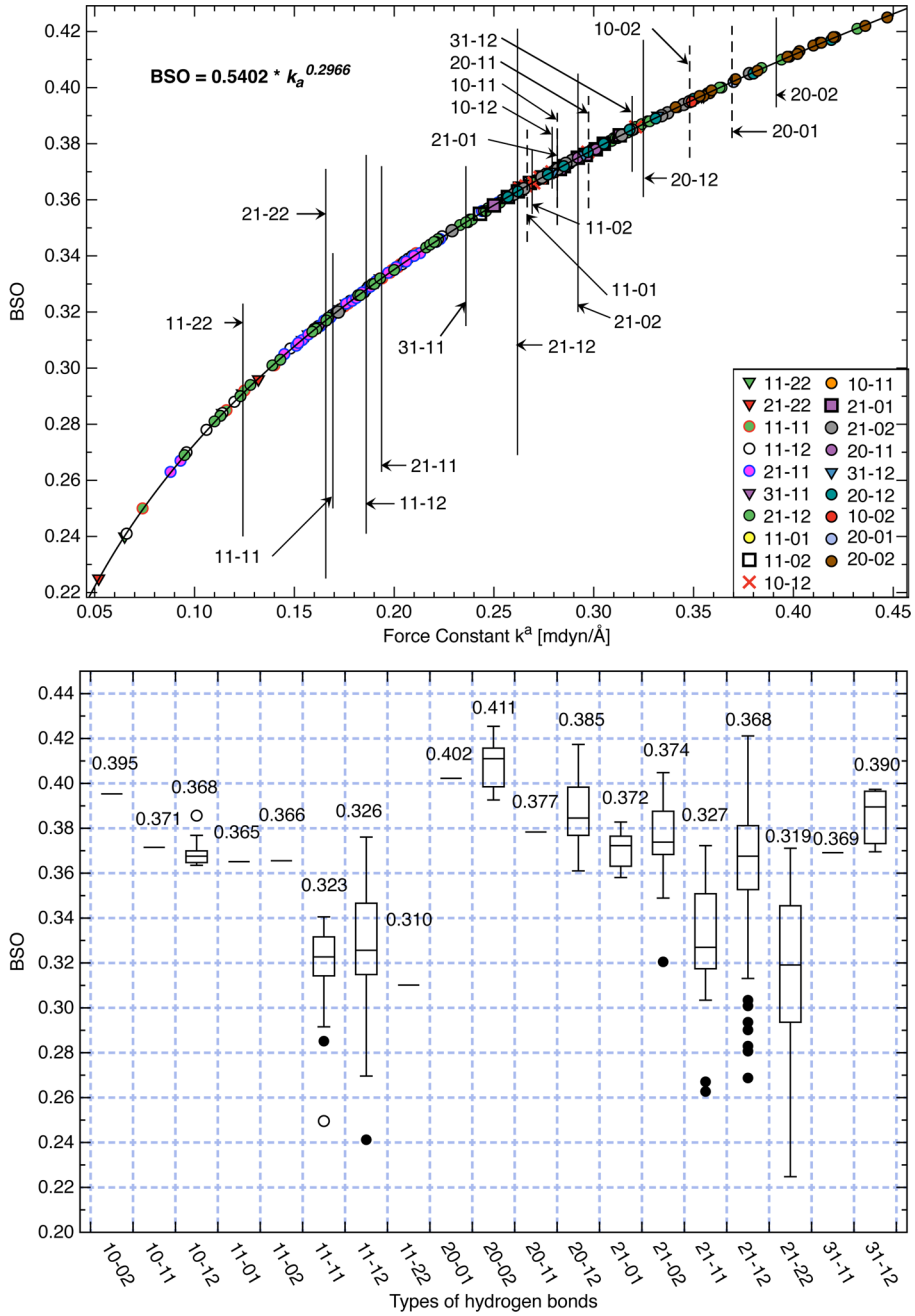

Figure 3. Top: The bond strength order (BSO) n of the H-bond given as a function of the local H-bond stretching force constant $k^a(H\cdots O)$. H-bonds are color-coded according to the notation of Figure 1. The average BSO value of each H-bond type is given by a vertical line where the length of the line indicates the range of BSO values found. Dashed vertical lines indicate those types of H-bonds for which only a few examples are observed. Bottom: The box-and-whisker diagram gives the statistical distribution of the BSO values for different types of H-bonds. For the definition of outliers (dots and circles), see Section 2.

type among the water molecules ((2,2) peripheral H-bonds) and accounts for just 1.4%. Other H-bonds such as 10-02 (0.3%), 10-11 (0.3%), 10-12 (2.6%), 11-01 (0.3%), 11-02 (1.4%), 11-22 (0.9%), 20-01 (0.3%), 20-11 (0.7%), 21-01 (2.6%), and 31-11 (1.0%) can only be found in one of the 50-mers. In summary, there is an exponential decay of the statistical occurrence of specific H-bonds with the number and position of peripheral H-bonds (see below), which holds if one considers all four 50-mers together (Figure 2).

Figure 3 provides an insight into which extent different H-bonds can be distinguished. The intrinsic strength of the H-bonds in the 50-mers as reflected by the BSO values varies by 50% from 0.225 to 0.425 (for comparison: 10-01 as in cyclic $(H_2O)_6$: n = 0.399). For each type of H-bond, the average BSO value is given by the crossing point of the curve $n(k^a)$ (top of Figure 3) and a vertical line, which defines the range of BSO values n for this particular type of H-bond by its length. In some cases, a definition of the range of n-values becomes meaningless because of the small number of H-bonds found for a particular type. Then, a dashed line of an arbitrary length of 0.04 BSO units is used. The representation at the top of Figure 3 is complemented by a statistical analysis of the different types of H-bonds among the 350 observed, which is given in the form

DOI: 10.1021/acs.jctc.6b00735
J. Chem. Theory Comput. 2017, 13, 55−76

of a box-and-whisker diagram (bottom of Figure 3; for an explanation, see Section 2).

The most stable H-bonds correspond to the 20-02 type (median: 0.411; average: 0.409; there is a linear relationship between median and average n values; R^2 = 0.96; see the SI). They are followed by the 20-01 H-bonds (0.402), 10-02 (0.395), and 20-12 H-bonds (0.385; blue dots in Figure 3). The green dots of the 21-12 H-bonds, which one could expect as the strongest H-bonds (6 peripheral H-bonds) are quite frequent but belong to the weaker H-bonds because of their large variation from 0.269 to 0.421 with many of these bonds being in the low strength range as a result of geometrical constraints. If the H-bonds are ordered according to the sequence given in Figure 1, a decline of the intrinsic H-bond strength from 10-02 to 11-12, an incline to 20-01 and 20-02, and another decline to 21-11 is found.

A H-bond turns out to be the strongest, which has just two external H-bonds on the D and two on the A side but which seems to guarantee both strong electrostatic and/or covalent interactions. This is is illustrated in Figure 1 for the 20-02 H-bond: Four peripheral water molecules polarize the electron density from A to D as is revealed by the difference density distribution $\Delta\rho(\mathbf{r})$ calculated for the 20-02 hexamer in Figure 4.

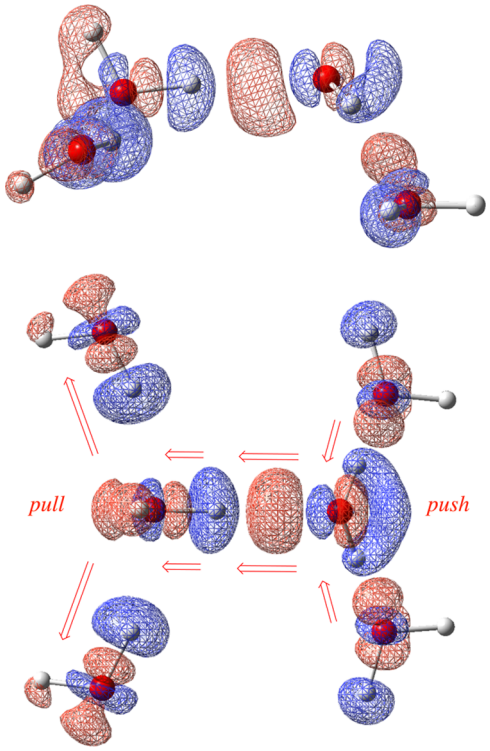

Figure 4. Diagrams show the difference density distribution $\Delta\rho(\mathbf{r})$ calculated for the 0.001 e/Bohr^3 density surface of the hexamer defining the 20-02 type of H-bonding (see Section 2, for details). Blue contour lines indicate a depletion, red an increase of the electron density distribution because of polarization. Top: side view. Bottom: bird view.

This is defined in the way that the extra-effect of the four peripheral H_2O molecules on the targeted 20-02 H-bond becomes visible. The two peripheral H_2O at the A side polarize with their lp electrons the O−H bonds of A thus leading to an increase in the density close to O1(A) and in the 20-02 H-bond region (*push-effect*, Figure 4). The two peripheral H_2O on the D-side support this effect by pulling density from the O2(D) lp orbitals toward their OH bonds thus helping to increase the polarization of the OH bond of the D molecule (*pull-effect*, Figure 4). Hence, the polarization of the electron density distribution is in the direction of the red arrows shown for the 20-02 H-bond in Figures 1 and 4.

At this point, it is appropriate to differentiate between physically based observables and the model quantities used in this work. Local mode frequencies and their associated force constants can be in principle measured.[91] This is also true for the electron density, whereas NPA charges are model quantities connected with a special orbital model.[81] Chemists explain H-bonding in terms of covalent, exchange, electrostatic, inductive, and dispersion interactions (see, e.g., Wang and co-workers[116]). Recently, Politzer and co-workers[117−119] pointed out that according to the Hellmann−Feynman theorem[120] noncovalent interactions are purely Coulombic in nature, and, accordingly, H-bonding might be described in this way. Although this is a valid view, often quantities such as NPA charges, charge transfer values, or charge delocalization energies provide a more detailed, model-based description of H-bonding. In this work, we will use the latter to describe covalent interactions. Difference densities can, as a result of their construction, reflect polarization effects although contributions from the changes in exchange repulsion, dispersion, etc. can also play a role. Apart from this, we will use an energy density based model that distinguishes just between covalent and electrostatic forces.[86,87,121]

Covalent versus Electrostatic H-Bonds. The covalent contribution of the H-bond can be considered as being dominated by a charge transfer from the lp(O1) orbital(s) to the $\sigma^*(O2-H)$ orbital of the D water (see bottom of Figure 5). The overlap between these orbitals will be maximal provided they are suitably oriented in line with an O2HO1 angle α close to 180° and an approach distance between (O2)H and O1 that is smaller than the sum of the van der Waals radii (1.2 + 1.52 Å[122]). Covalent contributions caused by charge transfer lead to H-bond stabilization as is reflected by the increase of the delocalization energy $\Delta E(del)$ with the BSO value (Figure 5, top), a more negative energy density at the H-bond critical point $\mathbf{r}_b$, and an accumulation of the electron density at this point.[86,87,121]

In the 50-mers investigated, the delocalization energies $\Delta E(del)$ vary from 8 to 32 kcal/mol, whereas the corresponding force constants vary from 0.29 to 0.41 mdyn/Å. It is striking that the $\Delta E(del)$ values fall into two groups (with the exception of that of type 10-11), which nicely correlate with the average BSO values (R^2 = 1.00 and 0.97; Figure 5): The stronger H-bonds are presented by the upper line, which seems to combine those H-bond types with $i_a(D) + l_d(A) > j_d(D) + k_a(A)$ due to $i_a = l_d = 2$ and $j_d + k_a \leq 1$. Those H-bond types, which do not fulfill these criteria, are represented by the dashed lower line in Figure 5 (top).

It seems that the strength of the various H-bond types is strongly influenced by the delocalization energy $\Delta E(del)$ where of course this is only valid for the 350 H-bonds of the four 50-mers in their equilibrium geometries and the NPA approach used. One of the referees mentioned that for certain geometries two lp(O) of the same O can contribute to $\Delta E(del)$ of one H-bond. The analysis applied in this work revealed that for 79 out of 350 H-bonds a second $lp(O) \rightarrow \sigma^*(OH)$ contribution larger than 3.0 kcal/mol (about one tenth of the first delocalization energy) was encountered, i.e. in 22.5% of all H-bonds, whereas

DOI: 10.1021/acs.jctc.6b00735
J. Chem. Theory Comput. 2017, 13, 55−76

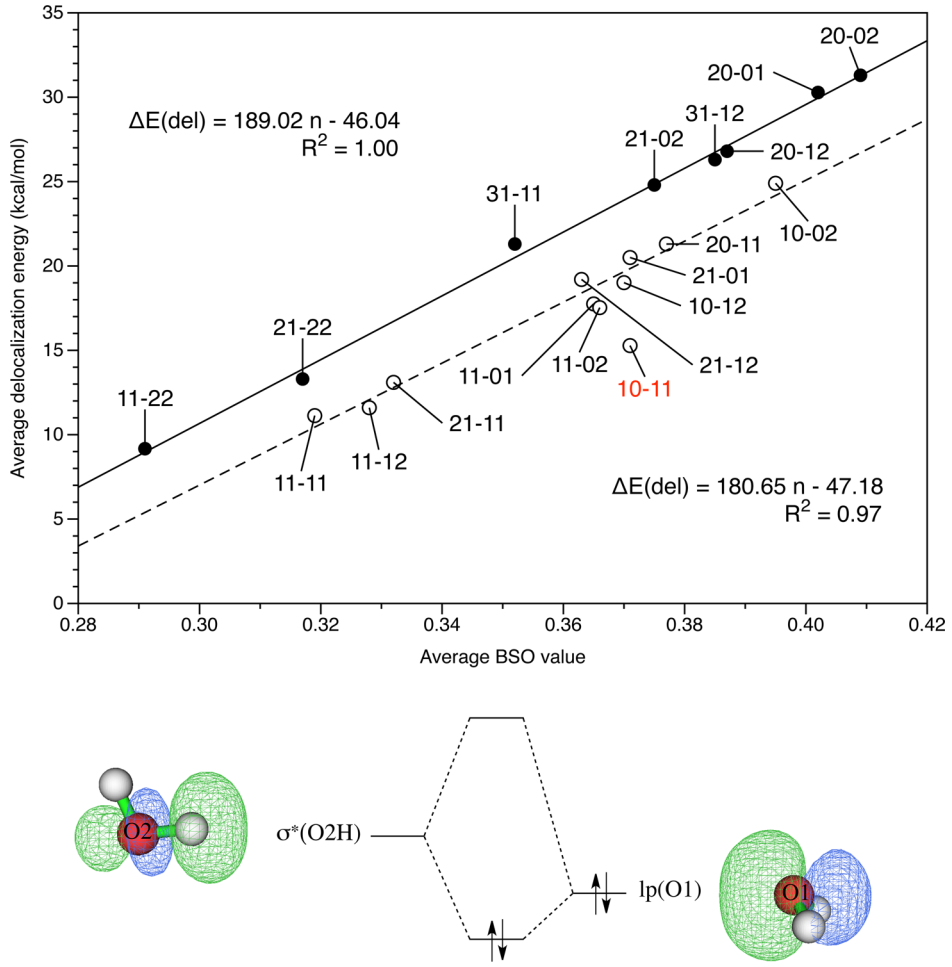

Figure 5. Top: The average delocalization energy $\Delta E(del) = \Delta E(lp(O) \rightarrow \sigma^*(OH))$ is plotted as a function of the average BSO n of the H-bond. For two different classes of H-bonds two correlation lines are obtained (not included: the 10-11 H-bond type). Bottom: The covalent contribution to the H-bond implies a delocalization of the lone pair (lp) electrons of atom O1 (green lobe of the orbital on the right) into the $\sigma^*(OH)$ antibonding orbital of the OH donor (green lobe of the orbital on the left). The energy stabilization caused by the charge transfer was determined by second order perturbation theory and is the basis for the delocalization energies of the upper diagram.

for 90% of all H-bonds the second lp contribution is between 0.05 and 3 kcal/mol. The perturbation theory analysis based on the NPA model also revealed that $\Delta E(del)$ contributions involving other than lp-orbitals are smaller than 0.1 kcal/mol, and therefore it is reasonable to use $\Delta E(del)$ for the description of the covalent contributions to the H-bond.

An increase of the average number of H-bonds, $m(AD)$, from 2 to 4 (Figure 1) does not necessarily weaken the H-bond but leads to a larger variation in the n-values because of stronger OH···O bending, the geometric limitations in the overlap between the lp(O1) and the σ^*(O2H) orbitals, a less than optimal charge transfer, and lower covalent contributions to H-bonding, which might be only partly compensated by electrostatic contributions (see 21-12 in Figures 3, top, and 6, top).

In Figure 6 (top), the geometrical conditions for H-bonding are compared. The box-and-whisker diagram gives the nonlinearity of the H-bond unit O2H···O1 as measured by the angle α. The analysis reveals that the stronger H-bonds (20-02, 10-02, etc.) are more linear in agreement with the requirements for maximal overlap and charge transfer. The 21-12 H-bonds have the largest variation in α (almost 40°, Figure 6). Noteworthy is that the median values are in the range from 164 to 173° irrespective of the H-bond considered. Since the nonlinearity of the H-bond arrangement is closely related to the covalent or electrostatic character of the H-bond, we show at the bottom of Figure 6 the statistical analysis of the energy density at the H-bond critical point, which should be negative for a dominant covalent bond according to the Cremer–Kraka criteria.[86−88] This is qualitatively confirmed by the diagram, which gives an "inverted" distribution of box-and-whisker units as compared to the diagrams in Figure 3. Accordingly, the 20-02 H-bond has the most negative energy density values, whereas the 21-12 H-bonds have at the same time the most positive energy density values and the largest variation of values.

Variation in the Strength of a H-Bond. The explanation why the 20-02 H-bond is the strongest one has been based on Figures 1 and 4 (polarization of the density as indicated by the red arrows). Any deviation from this optimal arrangement leads to a weakening of the H-bond. Using the average BSO values of Figure 3, the following ordering according to decreasing H-bond strength results: 20-02 > 10-01 > 20-01 > 10-02 > 20-12 > 20-11 > 21-02 > 10-11 ≈ 21-01 > 10-12 > 11-02 > 11-01 > 21-11 > 21-12 > 11-12 > 11-11 (For the cases, with a maximum of five H-bonds per water molecule: 31-12 > 31-11 > 21-22 > 11-22, see Figure 3). This ordering can qualitatively be reproduced if one considers that any competition of the

DOI: 10.1021/acs.jctc.6b00735
J. Chem. Theory Comput. 2017, 13, 55−76

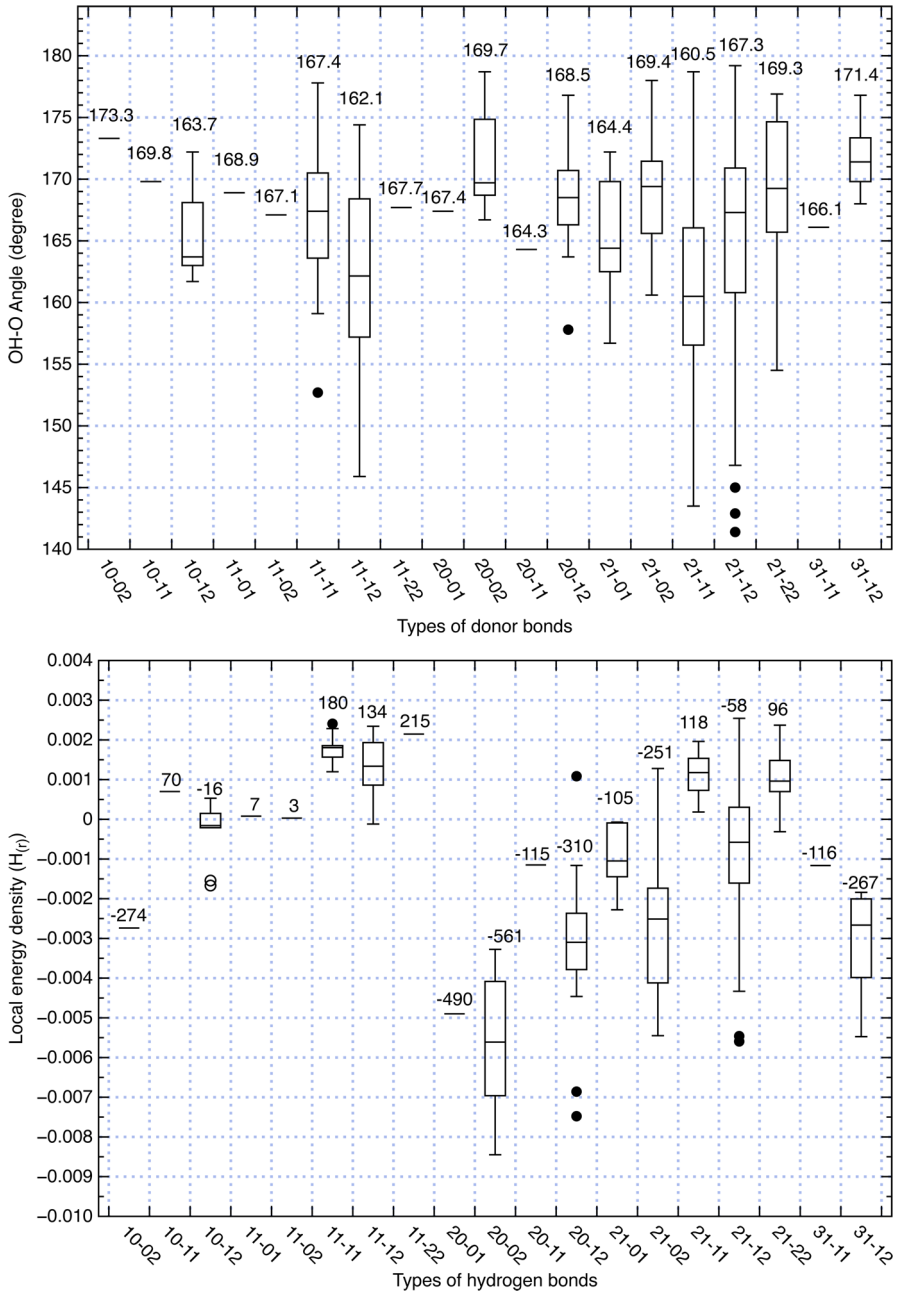

Figure 6. Top: The nonlinearity of the H-bond arrangement as measured by the angle α = O2H···O1 is analyzed in the form of a box-and-whisker diagram. For details of the box-and-whisker diagrams, see Section 2. Bottom: The box-and-whisker diagram gives the statistical distribution of the energy densities (given in Hartree/Bohr^3) at the H-bond critical point for different types of H-bonds. Median values given at the top of the upper whisker are multiplied by 10^5.

targeted H-bond with the second donor H-bond (as in 21-02, Figure 1) or with another external H-bond for the lp-density of the O(A) atom is a first order perturbation, whereas a change in the other peripheral H-bonds either on the D or A side can be considered as a second order perturbation (where perturbations on the D-side seem to have a somewhat larger effect than those on the A-side). Weighting first and second order perturbations qualitatively by −2 and −1 and using the short notation for the perturbation in the form $|(i_a, j_d, k_a, l_d) - (20\text{-}02)| = (p_i, p_j, p_k, p_l)$ (p: perturbation), the negative blue numbers in Figure 1 are obtained (at the upper right of each H-bond arrangement).

The qualitative comparison of a 21-11 H-bond with the 20-02 reference leads to a perturbation 01-11, which implies a weakening of −5 (two first order and one second order perturbation: $-2 \times 2 - 1 \times 1 = -5$) and thereby characterizes one of the weakest H-bonds (#14; in Figure 1. The ranking of each H-bond in terms of its average BSO is given by an encircled number: 1 gives the strongest and 16 the weakest H-bond; see also Figure 3). In this way, the ordering of most of the 16 H-bond types is correctly predicted (exceptions are 20-11 and 10-11; the 10-01 value is added in position 3 using the BSO of the cyclic hexamer $(H_2O)_6$). For example, the 10-02 H-bond has a perturbation value of 10-00, i.e. only one of the outer H-bonds is missing thus yielding a second order weakening of the targeted D−A H-bond of −1 and position 3 in the list of strong H-bonds.

DOI: 10.1021/acs.jctc.6b00735
J. Chem. Theory Comput. 2017, 13, 55−76

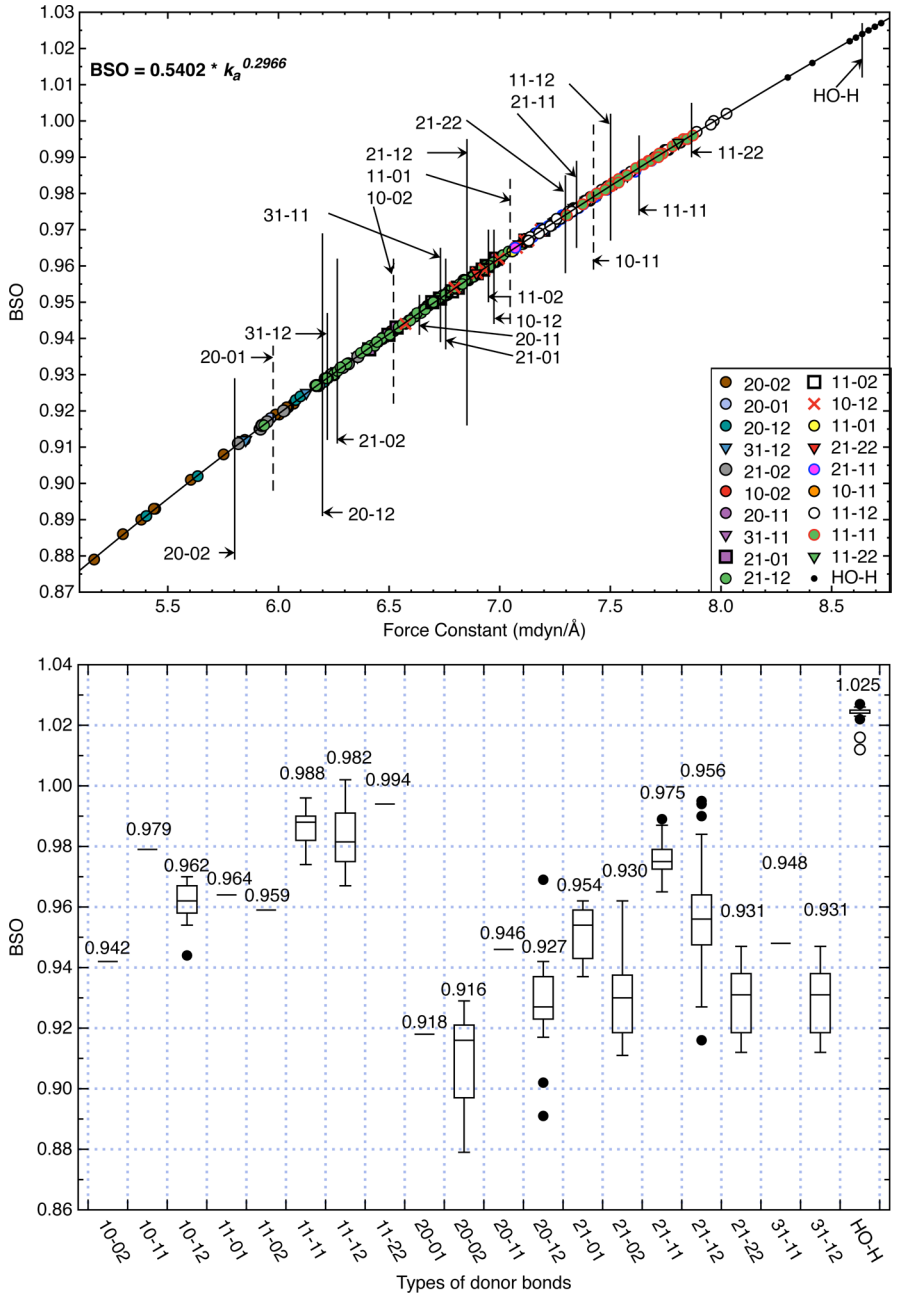

Figure 7. Top: The bond strength order (BSO) n of the O−H donor bond given as a function of the local O−H stretching force constant. Since each of these O−H-bonds is associated with a specific H-bond the former are identified and color-coded according to the associated H-bond (Figure 3). Bottom: A box-and-whisker diagram gives the statistical distribution of the BSO values of the various types of OH donor bonds leading to H-bonding in the four 50-mers investigated. For details of the box-and-whisker diagrams, see Section 2.

Utilizing the perturbation indices given for each type of H-bond, a distortion relationship between the rows of Figure 1 can be obtained (purple numbers on the left of Figure 1). According to these values (row 1: −1; row 2: −3; row 3:0; row 4: −2), H-bonds 20-rs (r = 0, 1; s = 1, 2) are the most stable ones, followed by those of row 1, whereas the least stable ones are found in row 2. This ordering is directly related to the possible perturbations of the 20-02 arrangement, which reduce its push−pull effect and thereby its covalent character.

The ordering of H-bonds by perturbation indices reveals that the polarization of the electron density of D and A as caused by the peripheral H_2O molecules (Figure 4) is an important electronic effect for the intrinsic strength of the H-bond. Polarization causes the energy of the σ^*(O2H) orbital being lowered and that of the lp(O1) being raised thus effectively decreasing the energy gap between these orbitals and increasing the delocalization energy $\Delta E(del)$. In addition, electrostatic interactions can be maximized by the polarization effect. The analyses summarized in Figures 3 (BSO-values), 5 (delocalization energies $\Delta E(del)$), and 6 (top: angles α; bottom: energy densities $H(\mathbf{r}_b)$) suggest that the covalent contributions to H-bonding are important for equilibrium geometries. This of course can be a consequence of (i) the finite size of the water clusters, (ii) the NPA model being used, and (iii) the exclusion of entropy effects in the current analysis.

DOI: 10.1021/acs.jctc.6b00735
J. Chem. Theory Comput. 2017, 13, 55−76

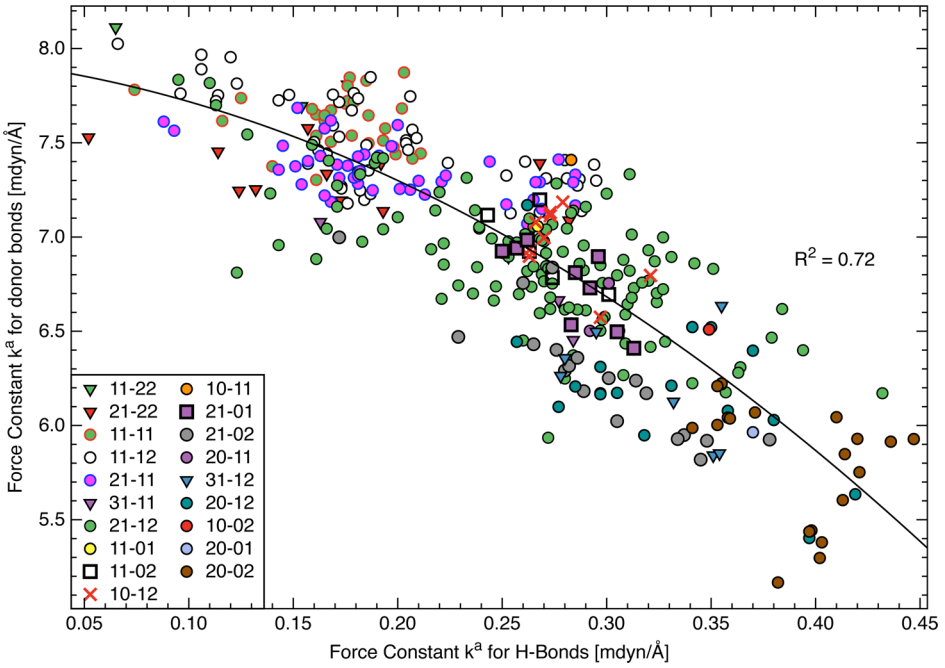

Figure 8. Testing the relationship between D and A: Comparison of the local stretching force constants $k^a(H\cdots O)$ and $k^a(O-H)$. The solid line is given by $k^a(O-H) = 7.938-1.211 \times k^a(H\cdots O) - 9.917 \times (k^a(H\cdots O))^2$ with $R^2 = 0.72$ and $\sigma = 0.30$ mdyn/Å. For the H-bond notation, see Figure 1.

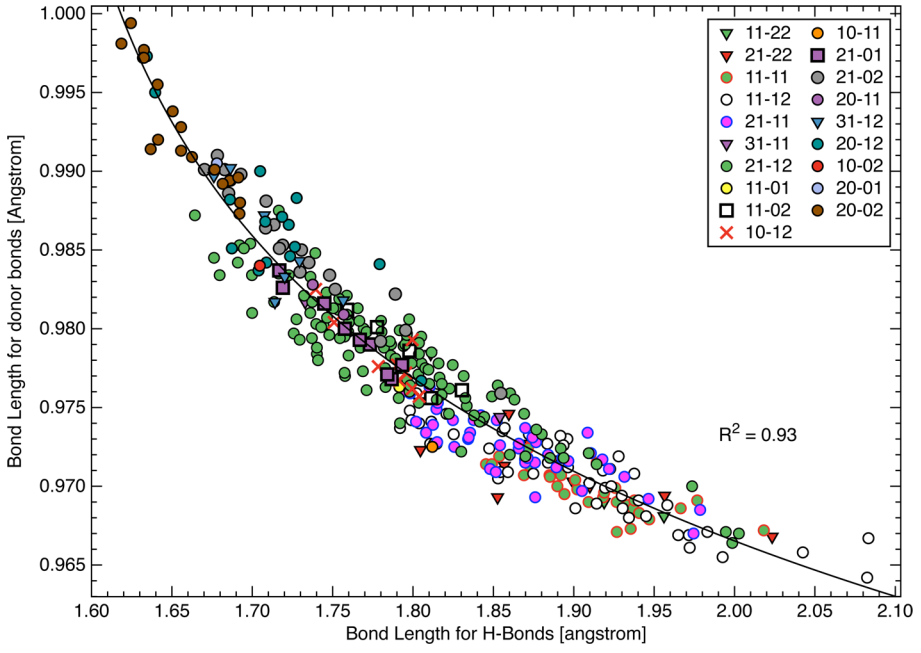

Figure 9. Testing the relationship between D and A: Comparison of the distance $R(H\cdots O)$ and $R(O-H)$. The solid line is given by $R(O-H) = 0.952-0.018 \times log[R(H\cdots O) - 1.552]$ with $R^2 = 0.93$ and $\sigma = 0.018$ Å. For the H-bond notation, see Figure 1.

Donor−Acceptor Relationships. There are numerous investigations, which use vibrational spectroscopy to describe H-bonding[123−136] and relate the strength of the O−H donor bond to the strength of the H-bond.[134,136,137] These investigations are mostly based on infrared spectroscopy as the weakening of the O−H donor bond in the case of H-bonding can be easily recorded by a red-shift of the OH stretching frequency. In a previous investigation, Freindorf and co-workers[59] have shown that the expected relationship between the O−H donor bond and the H-bond is not fulfilled. However, this investigation included many different H-bond donors. The current investigation is limited to D,A interactions between water molecules, and therefore a relationship between the O−H donor bond and the H-bond becomes more likely.

As shown in Figure 7 (top), the BSO values of the O−H donor bonds present in the four 50-mers vary from 0.88 to 1.00 (water molecule without any H-bonding) and beyond this to 1.03 if also those OH bonds are included that are on the outside of the water cluster and therefore not involved in any H-bonding (denoted HO−H in Figure 7). Although the range of BSO values is only one-third of that of the H-bonds, the same number of bonding situations as found for the H-bonds

DOI: 10.1021/acs.jctc.6b00735
J. Chem. Theory Comput. 2017, 13, 55−76

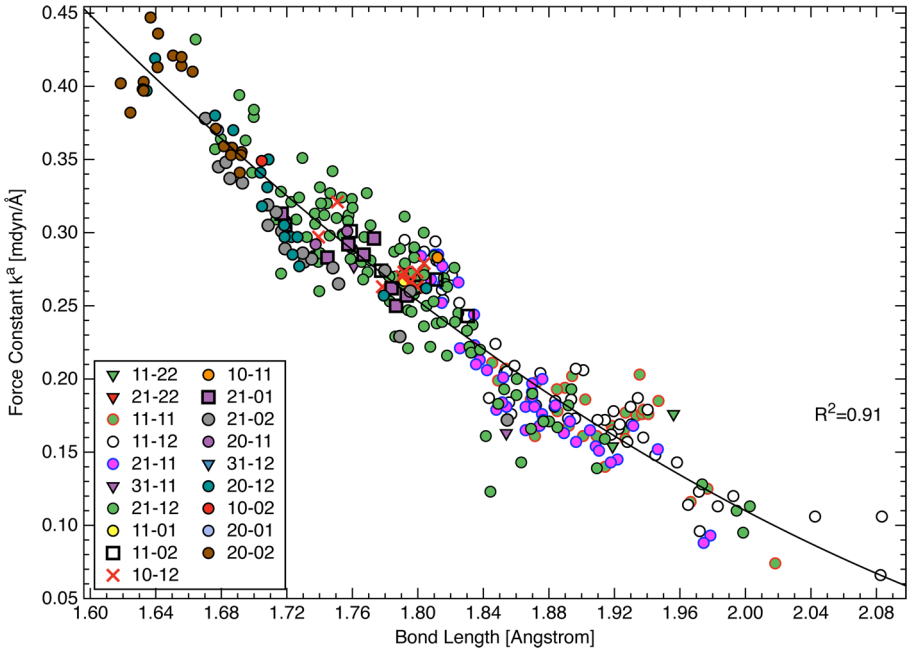

Figure 10. Testing the Badger relationship: Comparison of the local H-bond stretching force constant $k^a(H\cdots O)$ and the corresponding distance $R(H\cdots O)$. For the relationship $k^a = 0.648\ R(O\cdots H)^2 + 3.181\ R(O\cdots H) + 3.878$, $R^2 = 0.91$ and $\sigma = 0.023$ mdyn/Å are calculated. For the H-bond notation, see Figure 1.

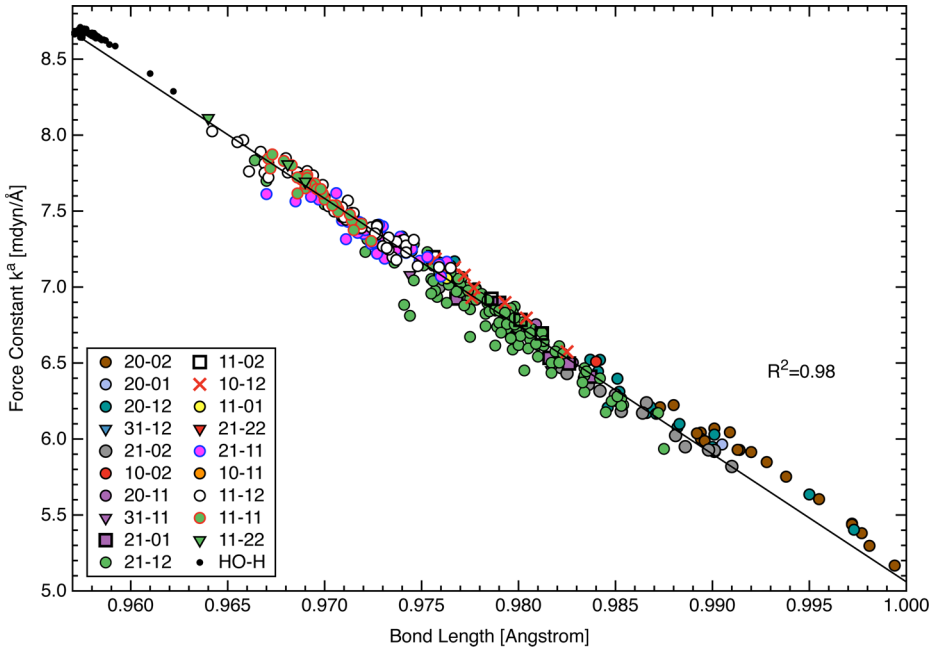

Figure 11. Testing the Badger relationship: Comparison of the local O−H stretching force constant $k^a(O{-}H)$ and the corresponding distance $R(O{-}H)$. For the relationship $k^a(O{-}H) = -84.095\ R(O{-}H) + 89.155$, $R^2 = 0.98$ and $\sigma = 0.087$ mdyn/Å result. For color code and notation, see Figures 1 and 7.

can be distinguished. Each is indicated in Figure 7 by a vertical solid or dashed line, which gives the average BSO value of a given O−H donor bond type that, for reasons of simplicity, is characterized by the H-bond it is engaged in.

There is a qualitative relationship between O−H donor bonds and H-bonds insofar as the weakest O−H donor bonds (see 20-02 in Figure 7) are associated with the strongest H-bonds and vice versa. This is in line with the covalent character of the strong H-bonds, which implies charge transfer from O2(lp) into the σ^*-orbital of the donor bond. Noteworthy is that the variation in the data points for the 20-02 donor bond is smaller than that for the corresponding H-bond, which again is a result of the fact that the first is primarily influenced by charge transfer and thereby a covalent weakening effect, whereas the latter is in addition influenced by electrostatic effects (for the calculated energy densities of the OH donor bonds, see the SI). Figure 7 also reveals that the various O−H donor bond types are much closer together with largely overlapping value ranges so that a differentiation on the basis of their average (Figure 7,

DOI: 10.1021/acs.jctc.6b00735
J. Chem. Theory Comput. 2017, 13, 55−76

Table 1. Comparison of the Total Numbers and Percentages of All Types of Hydrogen Bonds for 1000 $(H_2O)_{1000}$ Clusters Determined along the MD Trajectories and Calculated with the TIP5P Force Field for an NPT Ensemble at 283 and 363 K[a]

H-bond type	N(283)	%	N(363)	%	Δ	Δ1	Δ2
20-02	22015	1.4	25003	2.0	2988	13.6	0.6
20-01	12337	0.8	32003	2.6	19666	159.4	1.8
10-01	7585	0.5	46884	3.8	39299	518.1	3.3
10-02	13163	0.8	36261	2.9	23098	175.5	2.1
20-12	91754	5.6	37873	3.0	−53881	−58.7	−2.6
group (1)	146854	9.1	178024	14.3	31170	21.2	
20-11	37676	2.3	39254	3.2	1578	4.2	0.9
21-02	106723	6.6	46078	3.7	−60645	−56.8	−2.9
10-11	24033	1.5	61427	4.9	37394	155.6	3.4
21-01	57788	3.6	59326	4.8	1538	2.7	1.2
10-12	57310	3.5	58129	4.7	819	1.4	1.2
11-02	46680	2.9	54498	4.4	7818	16.7	1.5
group (2)	330210	20.4	318712	25.7	−11498	−3.5	
11-01	26433	1.6	71123	5.7	44690	169.1	4.1
21-12	471376	29.0	72019	5.8	−399357	−84.7	−23.2
21-11	184060	11.3	75541	6.1	−108519	−59.0	−5.2
11-12	210040	12.9	90199	7.2	−119841	−57.1	−5.7
11-11	85691	5.3	96990	7.8	11299	13.2	2.5
group (3)	977600	60.1	405872	32.6	−571728	−58.5	
groups (1+2+3)	1454664	89.6	902608	72.6	−552056	−38.0	
00-00	138	$<0.0_5$	3852	0.3	3714	2691.3	0.3
00-01	839	0.1	11926	1.0	11087	1321.5	0.9
00-02	1399	0.1	9271	0.7	7872	562.7	0.6
00-10	309	$<0.0_5$	4499	0.4	4190	1356.0	0.4
00-11	2696	0.2	16510	1.3	13814	512.4	1.1
00-12	6310	0.4	15468	1.2	9158	145.1	0.8
01-00	351	$<0.0_5$	5078	0.4	4727	1346.7	0.4
01-01	2311	0.1	15569	1.2	13258	573.7	1.1
01-02	3912	0.2	12064	1.0	8152	208.4	0.8
01-10	869	0.1	5874	0.5	5005	575.9	0.4
01-11	7554	0.5	22058	1.8	14504	192.0	1.3
01-12	17432	1.1	20618	1.7	3186	18.3	0.6
10-00	1197	0.1	14940	1.2	13743	1148.1	1.1
10-10	2630	0.2	16292	1.3	13662	519.5	1.1
11-00	3804	0.2	22891	1.8	19087	501.8	1.6
11-10	9641	0.6	25610	2.1	15969	165.6	1.5
20-00	1824	0.1	10046	0.8	8222	450.8	0.7
20-10	4060	0.2	10295	0.8	6235	153.6	0.6
21-00	8576	0.5	18875	1.5	10299	120.1	1.0
21-10	19580	1.2	19768	1.6	188	1.0	0.4
group (4)	95432	5.9	281504	22.6	186072	195.0	
22-00	32	$<0.0_5$	146	$<0.0_5$	114	356.3	$<0.0_5$
31-00	305	$<0.0_5$	846	0.1	541	177.4	0.1
22-01	205	$<0.0_5$	367	$<0.0_5$	162	79.0	$<0.0_5$
31-01	1960	0.1	2697	0.2	737	37.6	0.1
31-10	465	$<0.0_5$	754	0.1	289	62.2	0.1
22-10	93	$<0.0_5$	191	$<0.0_5$	98	105.4	$<0.0_5$
22-02	242	$<0.0_5$	286	$<0.0_5$	44	18.2	$<0.0_5$
31-02	3697	0.2	2217	0.2	−1480	−40.0	$<0.0_5$
22-11	628	$<0.0_5$	659	0.1	31	4.9	0.1
31-11	4541	0.3	2826	0.2	−1715	−37.8	−0.1
22-12	1212	0.1	533	$<0.0_5$	−679	−56.0	−0.1
31-12	11712	0.7	2849	0.2	−8863	−75.7	−0.5
group (5)	25092	1.4	14371	1.1	−10721	−42.7	
00-22	382	$<0.0_5$	1169	0.1	787	206.0	0.1
00-13	11	$<0.0_5$	82	$<0.0_5$	71	645.5	$<0.0_5$
01-22	1230	0.1	1624	0.1	394	32.0	$<0.0_5$
10-22	2915	0.2	3699	0.3	784	26.9	0.1
01-13	32	$<0.0_5$	94	$<0.0_5$	62	193.8	$<0.0_5$
10-13	130	$<0.0_5$	323	$<0.0_5$	193	148.5	$<0.0_5$

DOI: 10.1021/acs.jctc.6b00735
J. Chem. Theory Comput. 2017, 13, 55−76

Table 1. continued

H-bond type	$N(283)$	%	$N(363)$	%	Δ	Δ1	Δ2
11-13	441	$<0.0_5$	442	$<0.0_5$	1	0.2	$<0.0_5$
20-13	212	$<0.0_5$	211	$<0.0_5$	−1	−0.5	$<0.0_5$
20-22	3035	0.2	2008	0.2	−1027	−33.8	$<0.0_5$
12-22	163	$<0.0_5$	167	$<0.0_5$	4	2.5	$<0.0_5$
21-13	953	0.1	393	$<0.0_5$	−560	−58.8	−0.1
30-22	34	$<0.0_5$	48	$<0.0_5$	14	41.2	$<0.0_5$
group (6)	9538	0.6	10260	0.7	722	7.6	
22-22	224	$<0.0_5$	111	$<0.0_5$	−113	−50.4	$<0.0_5$
22-21	80	$<0.0_5$	70	$<0.0_5$	−10	−12.5	$<0.0_5$
31-22	286	$<0.0_5$	129	$<0.0_5$	−157	−54.9	$<0.0_5$
31-21	75	$<0.0_5$	93	$<0.0_5$	18	24.0	$<0.0_5$
group (7)	665	0.0	403	0.0	−262	−39.4	
groups (5+6+7)	35295	2.0	25034	1.8	−10261	−29.1	
group (8)	41475[b]	2.5	36534[c]	2.9	−4941	−11.9	
total	1626866	100.0	1245680	100.0	−381186	−30.6	

[a]In the first column the type of H-bonding is given in the short form introduced in the text. The table is partitioned into 5 groups: 1) 16 types of H-bonds discussed in connection with the 50-mers; 2) group 2 extends from 16 to the 36 standard types of H-bonds in general possible; 3) situations where the donor water (group 4), the acceptor water (group 5), or both (group 6) are involved in 5 H-bonds. $N(T)$ denotes the number of H-bonds at a given temperature T, Δ denotes the difference $N(363) - N(283)$, $\Delta 1 = 100[N(363) - N(283)]/N(283)$ is the percentage change of a given type of H-bond upon raising T to 363 K, $\Delta 2 = \eta(363) - \eta(283)$ is the difference between the percentage values $\eta = 100N(ij{-}kl)/N$ of a specific H-bond type at a certain T. [b]These groups include H-bond types with less than 0.05%, e.g., 00-03, 00-20, 00-21, 01-03, 01-20, 01-21, 01-23, 01-31, 01-32, 02-00, etc. (see Table S6, SI). [c]These groups include H-bond types with less than 0.05%. e.g. 00-03, 00-13, 00-14, 00-20, 00-21, 00-22, 00-23, 00-31, 00-32, 01-03, etc. (see Table S6, SI).

top) or median values (bottom) is difficult. Just 3 O−H donor bonds can be clearly distinguished (20-02, 20-01, HO-H).

In Figures 8 and 9, local stretching force constants k^a and distances R of the two interacting bonds are correlated. There is a quadratic relationship in the case of the force constants which is poorly fulfilled (R^2 = 0.72) thus revealing that the intrinsic strength of the O−H donor bond cannot provide a reliable measure for the intrinsic strength of the H-bond. Scattering of the data points is caused (among others) by those H-bonds involving 4-fold coordinated O atoms (e.g., green and purple dots both encircled in black).

For the corresponding distances, the scattering of data points is reduced (R^2 = 0.93, Figure 9), which might provide a basis to predict H-bond distances from known O−H bond lengths. The changes in the H-bond distance are 14 times larger than those in the O−H donor bond length. The corresponding force constants change as 1:7, which means that the R values are more sensitive than the corresponding k^a values in the case of the H-bonds, whereas the R-variation in the donor bonds is much smaller than that of the local force constants. This leads to the fact that the scattering is smaller (due to the smaller $R(O{-}H)$ variation) and a quantitative distance relationship can be found. The latter can be related to a change in the H-bond mechanism. For strong H-bonds, there is a linear relationship with a dominant covalent interaction between donor and acceptor bonds. For weak H-bonds, the electrostatic bonding mechanism becomes more important thus leading to a second linear R-relationship.

We conclude that the electrostatic contributions, especially in the case of the weak H-bonds, make it difficult (even in the case where covalent contributions are significant) to predict the properties of the H-bonds once those of the donor bonds are known. The fact that the O−H donor bond is primarily influenced by covalent effects and that the corresponding H-bonds are sensitive to both covalent and electrostatic effects is the reason why the corresponding force constants (or alternatively the BSO values) poorly correlate with each other. Previous claims to this extent were based on a small number of data points so that reliable conclusions could not be made.

Badger's Rule. The Badger rule implies that there is a power relationship between bond length and stretching force constant.[97] The rule was originally based on observations made for diatomic molecules[97,98] and was later generalized to covalent bonding in polyatomic molecules.[99] One might expect that the Badger rule is largely fulfilled for the OH donor bonds and less for the H-bonds themselves. Figures 10 and 11 show the two different situations.

There is a linear relationship between distance R and stretching force constant k^a in both cases, however associated with some scattering of data points in the case of the H-bonds (R^2= 0.91). Figure 10 reveals that the scattering is caused predominantly by the 21-12 H-bonds (green dots in black circles) and the H-bonds involving pentacoordinated O (triangles), but even for the strongly covalent 20-02 H-bonds (brown dots in black circles), a linear relationship between R and k^a cannot be obtained. Obviously, the generalized Badger rule is for H-bonding of limited value.

The situation is better in the cases of the covalent O−H donor bonds (Figure 11). Deviations from a linear relationship (R^2 = 0.98) are found again for the O−H bonds involved in 21-12 H-bonding (in short: 21-12 O−H bonds). In general, those bonds, which involve tetra- or pentacoordinated O atoms, lead to scattering.

WHY DOES WARM WATER FREEZE FASTER THAN COLD WATER?

The fact that warm water freezes faster than cold water is known in the literature as the Mpemba effect according to its first discovery by Mpemba.[138] This macroscopic phenomenon has been investigated many times and explained in many different ways referring, e.g., to the temperature gradient in the liquid, impurities in the water, dissolved oxygen and carbon dioxide, evaporation from the freezing liquid, difference in heat

DOI: 10.1021/acs.jctc.6b00735
J. Chem. Theory Comput. 2017, 13, 55−76

Table 2. Comparison of the Numbers and Percentages of Bifurcated Hydrogen Bonds Found for 1000 $(H_2O)_{1000}$ Clusters at 283 and 363 K[a]

H-bond type with bifurcation	N(283)	%	N(363)	%	Δ	Δ1	Δ2
22-00	32	$<0.0_5$	146	$<0.0_5$	114	356.3	$<0.0_5$
22-01	205	$<0.0_5$	367	$<0.0_5$	162	79.0	$<0.0_5$
22-10	93	$<0.0_5$	191	$<0.0_5$	98	105.4	$<0.0_5$
22-02	242	$<0.0_5$	286	$<0.0_5$	44	18.2	$<0.0_5$
22-11	628	$<0.0_5$	659	0.1	31	4.9	0.1
22-12	1212	0.1	533	$<0.0_5$	−679	−56.0	−0.1
group (4)	2412	0.1	2182	0.1	−230	−9.5	
12-22	163	$<0.0_5$	167	$<0.0_5$	4	2.5	$<0.0_5$
group (5)	163	$<0.0_5$	167	$<0.0_5$	4	2.5	
22-22	224	$<0.0_5$	111	$<0.0_5$	−113	−50.4	$<0.0_5$
22-21	80	$<0.0_5$	70	$<0.0_5$	−10	−12.5	$<0.0_5$
group (6)	304	$<0.0_5$	181	$<0.0_5$	−123	−40.5	
total (4+5+6)	2879	0.1	2530	0.1	−349	−12.1	

[a]For explanations, see Table 1. Bifurcated H-bonds can only be found for groups 4, 5, and 6 in Table 1.

loss, supercooling (lowering of liquid water below the freezing point), thermal convection currents, etc.[60−66] Most of these explanations had to be revoked, which had to do to some extent with the practical difficulties of having exact, reproducible conditions for the experiment (size, shape, and material of the freezer cabinet, circulation of air above the cooling liquid, properties of the cooling system; balancing of the volume, conditions of supercooling, etc.).[60−66]

Attempts have been made to explain the Mpemba effect with the help of MD simulations and by relating microscopic details to complex macroscopic phenomena such as the thermal convection or supercooling.[139] Analyzing the results of the MD simulations of liquid water as modeled by a cluster of 1000 water molecules at 283 and 363 K (with control calculations at 308 and 378 K) over a time of 2 ns and utilizing the insight gained into H-bonding we will offer here a molecular explanation of the Mpemba effect directly being based on the interplay of strong (mostly more covalent) and weak (mostly more electrostatic) contributions as they emerge from the four model clusters and the MD simulations (Tables 1, 2, Tables S9−S12 in the SI, Figures 12, 13).

A total of 1.627 (283 K), 1.496 (308 K), 1.246 (363 K), and 1.182 million H-bonds (378 K) has been investigated where the analysis at 283 and 363 K is presented here. Increasing the temperature T from 283 to 363 K leads to a decrease of the average number of H-bonds per water molecule, m_{av}, from 3.254 to 2.491. This decrease can be analyzed utilizing the various types of H-bonds found for the 50-mers where one has to consider that in liquid water there are more possibilities for H-bonding than in the equilibrium geometries of the 50-mers. The 36 possible H-bonds (see Figure S1 of the SI) are all found in the MD simulations of liquid water using $(H_2O)_{1000}$ clusters as suitable models for the analysis (see Table 1, Figure 12, and the SI). In the bar diagram of Figure 12 (top), the 16 types of H-bonds of Figure 1 are ordered according to the intrinsic strength calculated for the 50-mers, whereas the 20 remaining ones (bottom, group 4 in Table 1) are ordered according to Figure S1 in the SI. The latter include 11 types for which D or/and A water do not have any other H-bond than the targeted one, which means that these are throughout relatively weak H-bonds. Their numbers should increase when H-bonds are broken, for example as a result of a T increase. This is confirmed by the significant increase of the group 4 H-bonds at 363 K by 186072 (Table 1 and red bars in the lower part of Figure 12). In total, about 381000 H-bonds are lost for the increase in T.

Table 1 gives details on the distribution of H-bonds at the two different T values (for other T, see the SI). Almost 90% (1454664 H-bonds) of all H-bonds analyzed at 283 K belong to the 16-types discussed in connection with the 50-mers. If one uses the partitioning in strong, normal, and weak H-bonds discussed in Section 3, then 9.1% of all H-bonds (group 1 in Table 1: 20-02, 20-01, 10-01, 10-02, 20-12) can be considered as being strong and 60.1% as being weak (group 3 in Table 1: 11-01, 21-12, 21-11, 11-12, 11-11) whereas the rest of 20.4% is of normal strength (group 2 in Table 1).

5.9% (95432) of all H-bonds belong to the group of the 20 H-bond types with either terminal water (*dangling H-bonds*) or a change in the position of the peripheral H-bonds that disturbs the flow of charge from the A water to the D water (group 4 in Table 1). The latter is supported by $i_a0{-}0l_d$ combinations such as in 20-02 or 10-01 but hindered in $0j_d - 0l_d$ or $i_a0 - k_a0$ H-bond types as in 01-01, 10-10, etc. (see Figure S1).

Bifurcated H-Bonds and Unusual Coordination Numbers. If a H-bond is associated with two or more acceptor atoms O2, one speaks of bifurcated H-bonds.[107] We note that in the literature this term is used sometimes also for O atoms that have a coordination number higher than 4 (*penta- or hexacoordinated O*). We will not follow this more general use of the term but distinguish here clearly between bi- (tri)furcated H-bonds and H-bonds involving penta (hexa)-coordinated O atoms. For the former, we did not find any examples in the 50-mers. Using the distance criterion described in Section 2, some of the OH donor bonds had to be assigned to acceptor O atoms that were already hosting two H-bonds. This increased the coordination number to 5. Four different types of H-bonding involving pentacoordinated water molecules were observed, which according to their intrinsic strength can be ordered as follows: 31-12 (7) > 31-11 (3) > 21-22 (12) > 11-22 (3) (their numbers are given in parentheses; Figure 3).

Increase of the coordination number of the D atom O2 by increased acceptance of peripheral H-bonds leads to a strengthening of the targeted H-bond as the polarization of the charge distribution at O2 is increased (see 31-12 and 31-11 in the upper curve of Figure 5). This causes a stronger covalent contribution to the H-bond under investigation. However, if the targeted H-bond has to compete with two other H-bonds as in 21-22 or 11-22 for the lp(O1) electrons, a relatively weak H-

DOI: 10.1021/acs.jctc.6b00735
J. Chem. Theory Comput. 2017, 13, 55−76

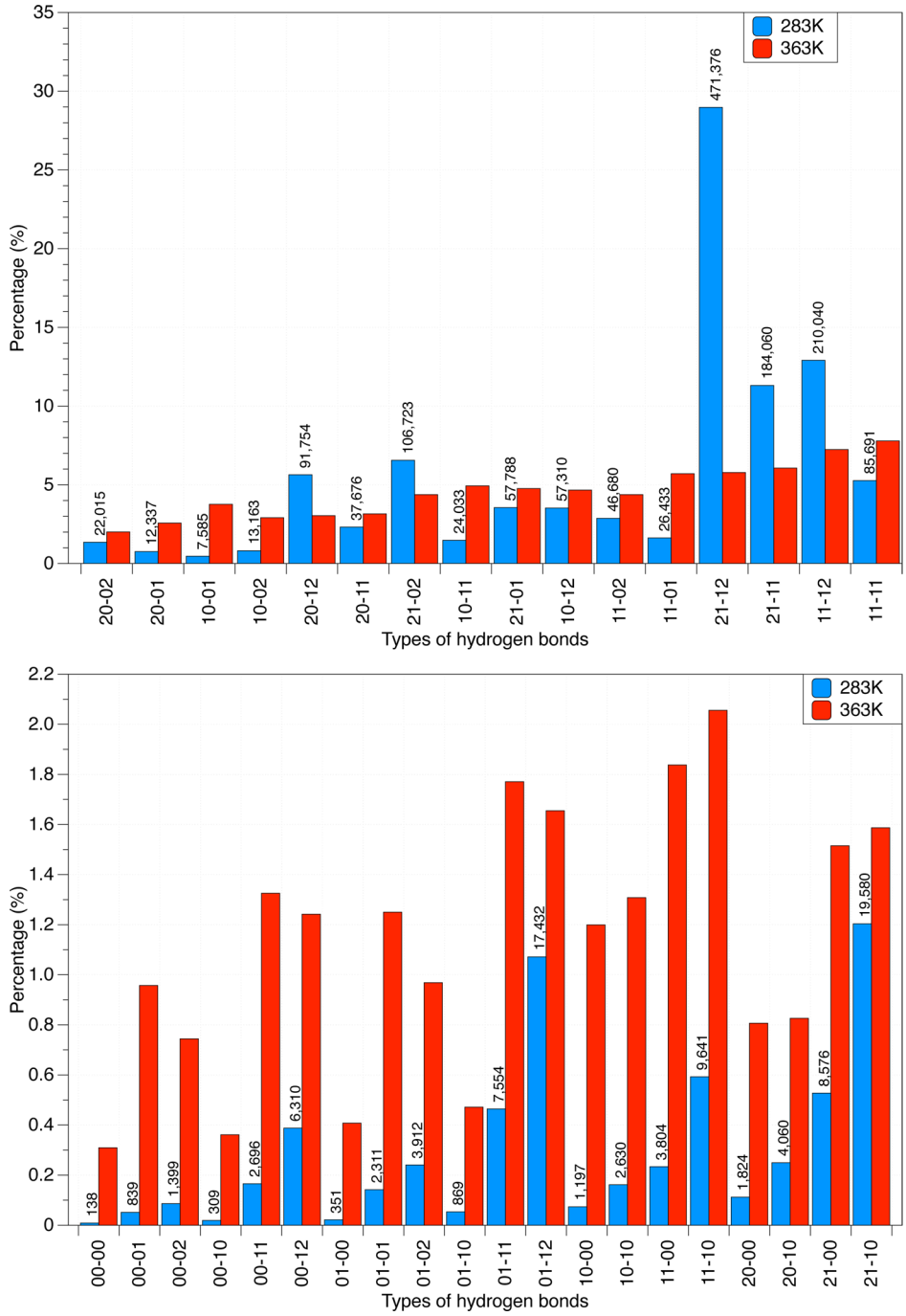

Figure 12. Percentages of the 36 types of different H-bonds in liquid water as modeled by 1000 $(H_2O)_{1000}$ clusters for the two different temperatures 283 (blue bars) and 363 K (red bars). The numbers at the blue bars give the actual H-bond count for a given type. Top: The 16 types of H-bonds discussed in connection with the 50-mers ordered according to strength. Bottom: The remaining 20 types of H-bonds not found for the 50-mers have all percentages ≤2%. See Figure S1 and Tables S9−S12 of the SI.

bond with a large variation in its BSO value due to electrostatic contributions results (Figure 5).

In the liquid water model used, all 36 + 71 = 107 different types of H-bonds with water containing pentacoordinated O (groups 5, 6, and 7 in Table 1; for a full account see Tables S7 and S8 of the SI) are found. Two different topologies can lead to pentacoordination: Either an O atom of the water molecule accepts 3 rather than 2 H-bonds (see above) or one of the donor H-bonds is bifurcated, i.e. it is equally H-bonded to two different O(A) atoms (Tables 2 and S8 of the SI). In the case of group 5, just 1.4% of the H-bonds (25092) is bifurcated, for group 6 just 9538 (0.6%), and for group 7 not more than 665 (Tables 2, S8, and Figure 13). Most of the 71 possible bifurcated H-bond types are found in the water model used (Table S8 of the SI) although their number (2969, Table S8) is relatively small.

The decrease in the average number of H-bonds with increasing T results from the fact that for higher T weak H-bonds such as 21-12 are cleaved (Figure 12, top right), which leads to the generation of fragments with terminal water (dangling H-bonds; Figure 12, bottom). Noteworthy is the fact that at 283 K only 2274 (0.22%) are not H-bonded (free),

DOI: 10.1021/acs.jctc.6b00735
J. Chem. Theory Comput. 2017, 13, 55−76

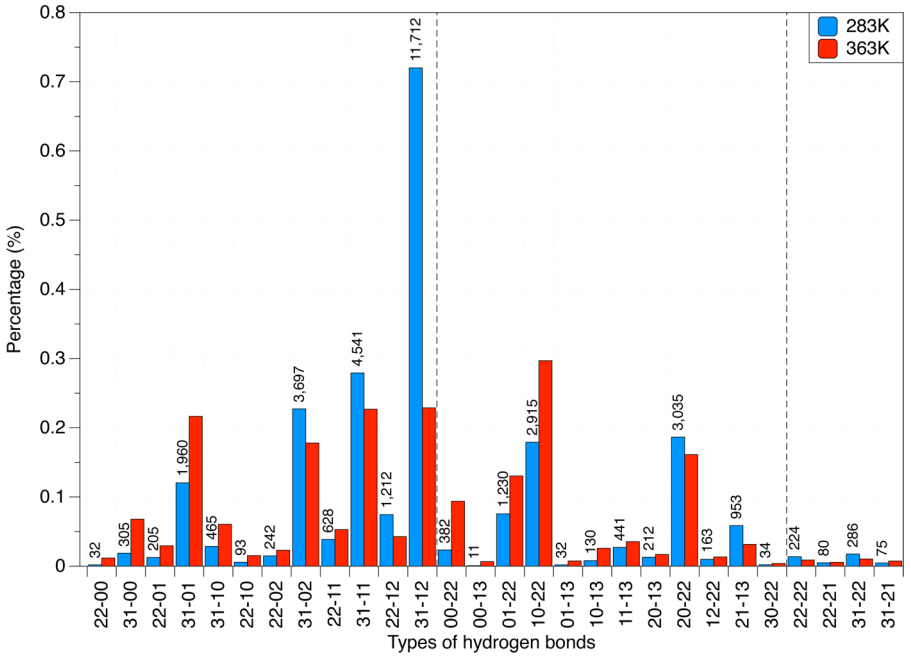

Figure 13. Percentages of bifurcated H-bonds in liquid water as modeled by 1000 $(H_2O)_{1000}$ clusters for the two different temperatures 283 (blue bars) and 363 K (red bars). The numbers at the blue bars give the actual H-bond count for a given type. First third up to dashed vertical line: D molecules with 5 H-bonds ($m(D) = 5$); second third: A molecules with $m(A) = 5$; last third: both D and A have $m = 5$. See Table 2.

whereas this number increases by a factor of 10 to 23494 (2.35%) at 363 K. Hence, the T increases substantially the number of water molecules with dangling H-bonds. The H-bonds being cleaved are, as found in this work, those with predominantly electrostatic nature. There is a significant increase in the percentages of the strong H-bond types (20-02, 20-01, 10-01, 10-02). This means that at higher T more water clusters with strong H-bonds remain (percentage-wise), whereas those with dangling H-bond increase, Figure 14), which can optimally recombine to form relatively strong covalent H-bonds as the geometrical prerequisites for covalent H-bonding are better fulfilled in smaller clusters.

The hexagonal lattice of ice is easily formed by these fragments because the fragments can easily adjust to the tetragonal environment of each O atom in solid ice (Figure 14). In cold water, the average number of H-bonds, m_{av} is higher. Both covalent and electrostatic H-bonds can be expected. The geometrical arrangement of the H-bonds is not optimal in those cases where both electrostatic and covalent bonding is possible (Figure 14). The electrostatic bonds have to be cleaved first and to rearrange before the water clusters can form the hexagonal ice lattice (Figure 14). This costs time and energy and is the reason why cold water freezes more slowly than warm water.

At this point, a caveat is necessary. The time scale of the nucleation process leading to the solid structure of ice is much larger than the time scale of H-bond cleavage or formation. However, cluster fragments with strong H-bonds are ideal for the nucleation process and thereby will accelerate freezing of water, whereas the larger m_{av} at lower T caused by a dense H-bond net with weak and strong H-bonds will slow down the nucleation process because weak, nonoptimal H-bonds have to be cleaved first. To prove this point MD simulations up to μs will be needed in the future.

CONCLUSIONS

The modeling of liquid water with 50-mers and 1000-mers using both quantum chemistry and MD simulation has led to a set of interesting results.

1) For the 50-mers investigated, a subset of 16 H-bond types (out of 36 possible H-bond types for a coordination number $c_O \leq 4$, excluding H-bond bifurcation) is sufficient to characterize the H-bond network of a 50-mer in its equilibrium geometry. For $c_O \leq 5$ (including pentacoordinated O with and without bifurcation), 36 + 71 = 107 additional H-bond types can be distinguished, which were found (with a few exceptions) among the 1.6 million H-bonds analyzed in the course of the MD simulations of this work. For the 50-mers, only a few H-bonds with $c_O = 5$ (25 out of 350) were identified, which involved pentacoordinated O atoms.

2) Utilizing the local stretching force constant and difference electron density distributions $\Delta\rho(\mathbf{r})$, we could determine the strongest type of H-bond to be the cooperative push−pull bond 20-02, which has an average BSO value of 0.41 and is, compared to the total range of BSO values from 0.22-0.42, at the upper limit of what seems to be possible in a water cluster. The push−pull effect of the peripheral water molecules has been verified by showing a suitably defined $\Delta\rho(\mathbf{r})$ calculated for the van der Waals surface of a 20-02 hexamer.

3) Any perturbation of the 20-02 H-bond by competition with other H-bonds (first order perturbations) or changing the pushing (pulling) H-bonds (second order perturbations) causes a weakening of the H-bond, which can be qualitatively analyzed. A rational explanation of the ordering of the H-bond types found in the 50-mers according to strength has been given in this work.

4) For the 50-mers, two linear relationships between the average intrinsic strength n and the average delocalization energy $\Delta E(del)$ (caused by charge transfer from lp(O1) to σ^*(O2H) ; Figures 3 and 5) could be derived. Since the charge transfer relates to the covalent character of a H-bond, it is

DOI: 10.1021/acs.jctc.6b00735
J. Chem. Theory Comput. 2017, 13, 55−76

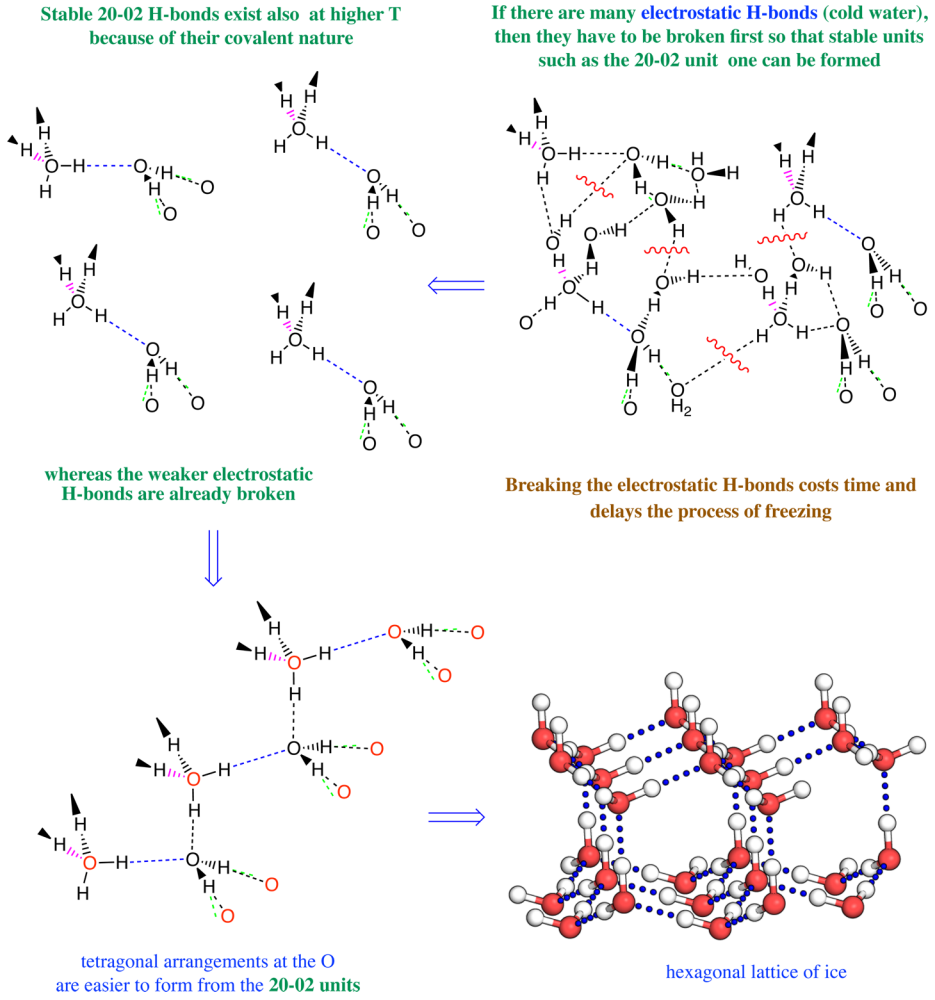

Figure 14. Explanation of the Mbempa effect: In warm water (upper left corner), weak, electrostatic H-bonds are already broken so that only those cluster units with strong covalent H-bonding exist, which more easily arrange (lower left corner) as is needed for the formation of the hexagonal ice lattice (lower right corner). In cold water (upper right corner), many electrostatic H-bonds (red wiggles) still exist, which have first to be broken to form the ice lattice, which costs time and energy.

reasonable to say that, within the model used, the covalent contributions influence the intrinsic strength of the various H-bond types. A rational has been given to explain the linear relationships; however, additional investigations are needed to verify the trends of $\Delta E(del)$ on a quantitative basis. An alternative measure is provided by the energy density at the H-bond critical points, which suggests that covalent and electrostatic interactions both play a role. With increasing nonlinearity of the H-bonding unit the electrostatic character increases.

5) Pentacoordination of an O atom does not necessarily lead to a weakening of the targeted H-bond. For example, converting a 21-12 H-bond into a 31-12 H-bond increases the polarization of the donor bond and thereby the cooperative effects so that the BSO value of the targeted H-bond raises by almost 21.6%. However, when the targeted H-bond gets a third competitor for the O1 electron lone pairs as for the 11-22 or 21-22 H-bonds, a significant weakening of the H-bond results.

6) In the MD simulations, almost all of the 107 additional H-bond types for $c_O = 5$ were found (together <4%) of which a subset of 0.1% was due to H-bond bifurcation.

7) For dominantly covalent H-bonds, there is an inverse relationship between the strength of the H-bond and that of the donor bond (Figure 8), which is of more qualitative nature. When using O−H and H···O distances, a more quantitative relationship results (Figure 9). The analysis reveals that there is a covalent and an electrostatic H-bonding mechanism active.

8) The Badger rule for the H-bonds and O−H donor bonds investigated is only semiquantitatively fulfilled where the 21-12 H-bonds are the major cause for data point scattering. Scattering is smaller for the relationship for the O−H donor bonds because the covalent character of H-bonding prevails in this case.

9) Based on the quantum chemical analysis of the 50-mers and the MD simulations leading to the investigation of 1.6 million H-bonds, the distribution of the most important H-bonds could be determined for different T and ordered according to their strength. This was possible because the majority of H-bonds identified belongs to the group analyzed for the 50-mers. The analysis of the MD simulation results leads us to propose a molecular explanation for the Mpemba effect. In warm water, the weaker H-bonds with predominantly electrostatic contributions are broken, and smaller water clusters with 20-02 or related strong H-bonding arrangements exist that accelerate the nucleation process that leads to the hexagonal lattice of solid ice. Therefore, warm water freezes faster than cold water in which the transformation from randomly arranged water clusters costs time and energy.

DOI: 10.1021/acs.jctc.6b00735
J. Chem. Theory Comput. 2017, 13, 55−76

Future studies prolonging the MD simulations to the μs range will help to verify the proposed molecular explanation of the Mpemba effect. Apart from this, the possibility of full-dimensional quantum simulations at a given T and a given pressure has to be considered.[55] There is also a necessity to provide further evidence for the push−pull effect of peripheral water molecules strengthening the targeted H-bond. Work is in progress to do this for the most frequent H-bond types.

■ ASSOCIATED CONTENT

Supporting Information

The Supporting Information is available free of charge on the ACS Publications website at DOI: 10.1021/acs.jctc.6b00735.

Distribution of H-bonds in the 50-mers (Table S1), H-bond properties calculated for the different 50-mers (Tables S2−S5); numbers and percentages of different H-bond types at different T values (Tables S6−S12), Cartesian coordinates (Tables S13−S14), presentation of all 36 different H-bonds (Figure S1), perspective drawings and numbering of atoms for all 50-mers (Figures S2−S5), box and whisker diagram for the distribution of the energy density of the OH donor bonds (Figure S6), analysis of the BSO values of the 50-mers (Figure S7) (PDF)

■ AUTHOR INFORMATION

Corresponding Author

*E-mail: dcremer@smu.edu.

ORCID

Dieter Cremer: 0000-0002-6213-5555

Notes

The authors declare no competing financial interest.

■ ACKNOWLEDGMENTS

We thank one of the referees for useful suggestions on how to extend and improve our investigation. This work was financially supported by the National Science Foundation, Grants CHE 1152357 and 1464906 and the National Science Foundation of China, Grant 21473087. We thank SMU for providing computational resources.

■ REFERENCES

(1) Pimentel, G. C.; McClellan, A. L. *The Hydrogen Bond*; W.H. Freeman: San Francisco, 1960.

(2) Jeffrey, G. A.; Saenger, W. *Hydrogen bonding in biological structures*; Springer-Verlag: Berlin, 1994.

(3) Stone, A. *The Theory of Intermolecular Forces*; Clarendon: Oxford, 1997.

(4) Scheiner, S. *Hydrogen Bonding: A Theoretical Perspective*; Oxford University Press: New York, 1997.

(5) Grabowski, S. J. E. *Hydrogen Bonding - New Insights, in Challenges and Advances in Computational Chemistry and Physics*; Springer: New York, 2006.

(6) Gilli, G.; Gilli, P. *The Nature of the Hydrogen Bond- IUCr Monographs on Crystallography - 23*; Oxford University Press: New York, 2009.

(7) Keutsch, F. N.; Saykally, R. J. Water clusters: Untangling the mysteries of the liquid, one molecule at a time. *Proc. Natl. Acad. Sci. U. S. A.* **2001**, *98*, 10533−10540.

(8) Morokuma, K.; Pedersen, L. Molecular-Orbital Studies of Hydrogen Bonds. An Ab Initio Calculation for Dimeric H_2O. *J. Chem. Phys.* **1968**, *48*, 3275−3282.

(9) Kollman, P. A.; Allen, L. C. Theory of the Hydrogen Bond: Electronic Structure and Properties of the Water Dimer. *J. Chem. Phys.* **1969**, *51*, 3286−3293.

(10) Diercksen, G. H. F. SCF MO LCGO studies on hydrogen bonding. The water dimer. *Chem. Phys. Lett.* **1969**, *4*, 373−375.

(11) Morokuma, K.; Winick, J. R. Molecular-Orbital Studies of Hydrogen Bonds. Dimeric H_2O with the Slater Minimal Basis. *J. Chem. Phys.* **1970**, *52*, 1301−1306.

(12) Hankins, D.; Moskowitz, J. W.; Stillinger, F. H. Water Molecule Interactions. *J. Chem. Phys.* **1970**, *53*, 4544−4554.

(13) Del Bene, J.; Pople, J. Theory of Molecular Interactions. I. Molecular Orbital Studies of Water Polymers Using a Minimal Slater-Type Basis. *J. Chem. Phys.* **1970**, *52*, 4858−4866.

(14) Diercksen, G. H. F. SCF MO LCGO studies on hydrogen bonding. The water dimer. *Theor. Chim. Acta* **1971**, *21*, 335−367.

(15) Del Bene, J. E. Theoretical Study of Open Chain Dimers and Trimers Containing CH_3OH and H_2O. *J. Chem. Phys.* **1971**, *55*, 4633−4636.

(16) Popkie, H.; Kistenmacher, H.; Clementi, E. Study of the structure of molecular complexes. IV. The Hartree-Fock potential for the water dimer and its application to the liquid state. *J. Chem. Phys.* **1973**, *59*, 1325−1336.

(17) Matsuoka, O.; Clementi, E.; Yoshimine, M. CI study of the water dimer potential surface. *J. Chem. Phys.* **1976**, *64*, 1351−1361.

(18) Tschumper, G. S.; Leininger, M. L.; Hoffman, B. C.; Valeev, E. F.; Schaefer, H. F.; Quack, M. Anchoring the Water Dimer Potential Energy Surface with Explicitly Correlated Computations and Focal Point Analyses. *J. Chem. Phys.* **2002**, *116*, 690−701.

(19) Kalescky, R.; Zou, W.; Kraka, E.; Cremer, D. Local Vibrational Modes of the Water Dimer - Comparison of Theory and Experiment. *Chem. Phys. Lett.* **2012**, *554*, 243−247.

(20) Lane, J. R. CCSDTQ Optimized Geometry of Water Dimer. *J. Chem. Theory Comput.* **2013**, *9*, 316−323.

(21) Pugliano, N.; Saykally, R. Measurement of Quantum Tunneling Between Chiral Isomers of the Cyclic Water Trimer. *Science* **1992**, *257*, 1937−1940.

(22) Mó, O.; Yanez, M.; Elguero, J. Cooperative (non-pairwise) effects in water trimers: An ab initio molecular orbital study. *J. Chem. Phys.* **1992**, *97*, 6628−6638.

(23) Schütz, M.; Bürgi, T.; Leutwyler, S.; Bürgi, H. B. Fluxionality and low-lying transition structures of the water trimer. *J. Chem. Phys.* **1993**, *99*, 5228−5238.

(24) Wales, D. J. Theoretical Study of Water Trimer. *J. Am. Chem. Soc.* **1993**, *115*, 11180−11190.

(25) Liu, K.; Loeser, J.; Elrod, M.; Host, B.; Rzepiela, J.; Pugliano, N.; Saykally, R. Dynamics of Structural Rearrangements in the Water Trimer. *J. Am. Chem. Soc.* **1994**, *116*, 3507−3512.

(26) Schütz, M.; Klopper, W.; Lüthi, H.-P. Low-lying stationary points and torsional interconversions of cyclic $(H_2O)_4$: An *ab initio* study. *J. Chem. Phys.* **1995**, *103*, 6114−6126.

(27) Fowler, J. E.; Schaefer, H. F., III Detailed Study of the Water Trimer Potential Energy Surface. *J. Am. Chem. Soc.* **1995**, *117*, 446−452.

(28) Wales, D.; Walsh, T. Theoretical study of the water pentamer. *J. Chem. Phys.* **1996**, *105*, 6957−6971.

(29) Wales, D.; Walsh, T. Theoretical study of the water tetramer. *J. Chem. Phys.* **1997**, *106*, 7193−7207.

(30) Taketsugu, T.; Wales, D. Theoretical study of rearrangements in water dimer and trimer. *Mol. Phys.* **2002**, *100*, 2793−2706.

(31) Anderson, J. A.; Crager, K.; Fedoroff, L.; Tschumper, G. S. Anchoring the Potential Energy Surface of the Cyclic Water Trimer. *J. Chem. Phys.* **2004**, *121*, 11023−11029.

(32) Pérez, J.; Hadad, C.; Restrepo, A. Structural Studies of the Water Tetramer. *Int. J. Quantum Chem.* **2008**, *108*, 1653−1659.

(33) Shields, R. M.; Temelso, B.; Archer, K. A.; Morrell, T. E.; Shields, G. C. Accurate Predictions of Water Cluster Formation, $(H_2O)_{n=2-10}$. *J. Phys. Chem. A* **2010**, *114*, 11725−11737.

(34) Ramírez, F.; Hadad, C.; Guerra, D.; David, J.; Restrepo, A. Structural studies of the water pentamer. *Chem. Phys. Lett.* **2011**, *507*, 229−233.
(35) Temelso, B.; Archer, K.; Shields, G. Benchmark Structures and Binding Energies of Small Water Clusters with Anharmonicity Corrections. *J. Phys. Chem. A* **2011**, *115*, 12034−12046.
(36) Temelso, B.; Shields, G. C. The Role of Anharmonicity in Hydrogen-Bonded Systems: The Case of Water Clusters. *J. Chem. Theory Comput.* **2011**, *7*, 2804−2817.
(37) Howard, J. C.; Tschumper, G. S. Wavefunction methods for the accurate characterization of water clusters. *WIREs Comput. Mol. Sci.* **2014**, *4*, 199−224.
(38) Fanourgakis, G.; Apra, E.; de Jong, W.; Xantheas, S. High-level ab-initio calculations for the four low-lying families of minima of $(H_2O)_{20}$: II. Spectroscopic signatures of the dodecahedron, fused cubes, face-sharing pentagonal prisms, and edge-sharing pentagonal prisms hydrogen bonding networks. *J. Chem. Phys.* **2005**, *122*, 134304.
(39) Bryantsev, V.; Diallo, M.; van Duin, A.; Goddard, W. Evaluation of B3LYP, X3LYP, and M06-Class Density Functionals for Predicting the Binding Energies of Neutral, Protonated, and Deprotonated Water Clusters. *J. Chem. Theory Comput.* **2009**, *5*, 1016−1026.
(40) Parthasarathi, R.; Elango, M.; Subramanian, V.; Sathyamurthy, N. Structure and Stability of Water Chains $(H_2O)_n$, n = 5−20. *J. Phys. Chem. A* **2009**, *113*, 3744−3749.
(41) Yang, F.; Wang, X.; Yang, M.; Krishtal, A.; van Alsenoy, C.; Delarue, P.; Senet, P. Effect of hydrogen bonds on polarizability of a water molecule in $(H_2O)_n$ (n = 6, 10, 20) isomers. *Phys. Chem. Chem. Phys.* **2010**, *12*, 9239.
(42) Iwata, S. Analysis of hydrogen bond energies and hydrogen bonded networks in water clusters $(H_2O)_{20}$ and $(H_2O)_{25}$ using the charge-transfer and dispersion terms. *Phys. Chem. Chem. Phys.* **2014**, *16*, 11310.
(43) Lenz, A.; Ojamae, L. Theoretical IR Spectra for Water Clusters $(H_2O)_n$ (n = 6−22, 28, 30) and Identification of Spectral Contributions from Different H-Bond Conformations in Gaseous and Liquid Water. *J. Phys. Chem. A* **2006**, *110*, 13388−13393.
(44) Bako, I.; Mayer, I. Hierarchy of the Collective Effects in Water Clusters. *J. Phys. Chem. A* **2016**, *120*, 631−638.
(45) Elango, M.; Subramanian, V.; Sathyamurthy, N. Structure and stability of spiro-cyclic water clusters. *J. Chem. Sci.* **2009**, *121*, 839−848.
(46) Sahu, N.; Khire, S.; Gadre, S. Structures, energetics and vibrational spectra of $(H_2O)_{32}$ clusters: a journey from model potentials to correlated theory. *Mol. Phys.* **2015**, *113*, 2970−2979.
(47) Qian, P.; Song, W.; Lu, L.; Yang, Z. Ab initio investigation of water clusters $(H_2O)_n$ (n = 2−34). *Int. J. Quantum Chem.* **2009**, *110*, 1924−1937.
(48) Huang, L.; Lambrakos, S.; Shabaev, A.; Bernstein, N.; Massa, L. Molecular analysis of water clusters: Calculation of the cluster structures and vibrational spectrum using density functional theory. *C. R. Chim.* **2015**, *18*, 516−524.
(49) Liu, J.; Wang, L.; Zhao, J. Density Functional Theory Calculations of Water Fullerenes: $(H_2O)_n$ Clusters with n = 20−40. *J. Comput. Theor. Nanosci.* **2009**, *6*, 454−458.
(50) Ludwig, R.; Appelhagen, A. Calculation of Clathrate-Like Water Clusters Including H_2O-Buckminsterfullerene. *Angew. Chem., Int. Ed.* **2005**, *44*, 811−815.
(51) Neela, Y.; Mahadevi, A.; Sastry, G. Hydrogen Bonding in Water Clusters and Their Ionized Counterparts. *J. Phys. Chem. B* **2010**, *114*, 17162−17171.
(52) Frigato, T.; VandeVondele, J.; Schmidt, B.; Schutte, C.; Jungwirth, P. Ab Initio Molecular Dynamics Simulation of a Medium-Sized Water Cluster Anion: From an Interior to a Surface-Located Excess Electron via a Delocalized State. *J. Phys. Chem. A* **2008**, *112*, 6125−6133.
(53) Loboda, O.; Goncharuk, V. Theoretical study on icosahedral water clusters. *Chem. Phys. Lett.* **2010**, *484*, 144−147.
(54) Turi, L. Hydration dynamics in water clusters via quantum molecular dynamics simulations. *J. Chem. Phys.* **2014**, *140*, 204317.
(55) Wang, Y.; Babin, V.; Bowman, J.; Paesani, F. The Water Hexamer: Cage, Prism, or Both. Full Dimensional Quantum Simulations Say Both. *J. Am. Chem. Soc.* **2012**, *134*, 11116−11119.
(56) Konkoli, Z.; Cremer, D. A New Way of Analyzing Vibrational Spectra. I. Derivation of Adiabatic Internal Modes. *Int. J. Quantum Chem.* **1998**, *67*, 1.
(57) Konkoli, Z.; Cremer, D. A New Way of Analyzing Vibrational Spectra. III. Characterization of Normal Vibrational Modes in Terms of Internal Vibrational Modes. *Int. J. Quantum Chem.* **1998**, *67*, 29.
(58) Zou, W.; Kalescky, R.; Kraka, E.; Cremer, D. Relating Normal Vibrational Modes To Local Vibrational Modes With The Help of an Adiabatic Connection Scheme. *J. Chem. Phys.* **2012**, *137*, 084114.
(59) Freindorf, M.; Kraka, E.; Cremer, D. A Comprehensive Analysis of Hydrogen Bond Interactions Based on Local Vibrational Modes. *Int. J. Quantum Chem.* **2012**, *112*, 3174−3187.
(60) Ahtee, M. Investigation into the Freezing of Liquids. *Phys. Educ.* **1969**, *4*, 379−380.
(61) Firth, I. Cooler? *Phys. Educ.* **1971**, *6*, 32−41.
(62) Kell, G. The Freezing of Hot and Cold Water. *Am. J. Phys.* **1969**, *37*, 564−565.
(63) Auerbach, D. Supercooling and the Mpemba effect: When hot water freezes quicker than cold. *Am. J. Phys.* **1995**, *63*, 882−885.
(64) Wojciechowski, B. Freezing of Aqueous Solutions Containing Gases. *Cryst. Res. Technol.* **1988**, *23*, 843−8.
(65) Brewster, R.; Gebhart, B. An experimental study of natural convection effects on downward freezing of pure water. *Int. J. Heat Mass Transfer* **1988**, *31*, 331−348.
(66) van der Elsken, J. The Freezing of Supercooled Water. *J. Mol. Struct.* **1991**, *250*, 245−251.
(67) Chai, J. D.; Head-Gordon, M. Long-range Corrected Hybrid Density Functionals with Damped Atom-Atom Dispersion Corrections. *Phys. Chem. Chem. Phys.* **2008**, *10*, 6615−6620.
(68) Chai, J. D.; Head-Gordon, M. Systematic Optimization of Long-Range Corrected Hybrid Density Functionals. *J. Chem. Phys.* **2008**, *128*, 084106−15.
(69) Thanthiriwatte, K. S.; Hohenstein, E. G.; Burns, L. A.; Sherrill, C. D. Assessment of the Performance of DFT and DFT-D Methods for Describing Distance Dependence of Hydrogen-Bonded Interactions. *J. Chem. Theory Comput.* **2011**, *7*, 88−96.
(70) Kozuch, S.; Martin, J. M. L. Halogen Bonds: Benchmarks and Theoretical Analysis. *J. Chem. Theory Comput.* **2013**, *9*, 1918−1931.
(71) Bauzá, A.; Alkorta, I.; Frontera, A.; Elguero, J. On the Reliability of Pure and Hybrid DFT Methods for the Evaluation of Halogen, Chalcogen, and Pnicogen Bonds Involving Anionic and Neutral Electron Donors. *J. Chem. Theory Comput.* **2013**, *9*, 5201−5210.
(72) Scheiner, S. Extrapolation to the Complete Basis Set Limit for Binding Energies of Noncovalent Interactions. *Comput. Theor. Chem.* **2012**, *998*, 9−13.
(73) Ditchfield, D.; Hehre, W.; Pople, J. Self-Consistent Molecular Orbital Methods. 9. Extended Gaussian-type basis for molecular-orbital studies of organic molecules. *J. Chem. Phys.* **1971**, *54*, 724.
(74) Hariharan, P.; Pople, J. The influence of polarization functions on molecular orbital hydrogenation energies. *Theor. Chim. Acta* **1973**, *28*, 213−222.
(75) Clark, T.; Chandrasekhar, J.; Spitznagel, G. W.; Schleyer, P. v. R. Efficient diffuse function-augmented basis sets for anion calculations. III. The 3-21+G basis set for first-row elements, Li-F. *J. Comput. Chem.* **1983**, *4*, 294−301.
(76) Li, W.; Li, S.; Jiang, Y. Generalized Energy-Based Fragmentation Approach for Computing the Ground-State Energies and Properties of Large Molecules. *J. Phys. Chem. A* **2007**, *111*, 2193−2199.
(77) Li, S.; Li, W.; Ma, J. Generalized Energy-Based Fragmentation Approach and Its Applications to Macromolecules and Molecular Aggregates. *Acc. Chem. Res.* **2014**, *47*, 2712−2720.
(78) Yang, Z.; Hua, S.; Hua, W.; Li, S. Low-Lying Structures and Stabilities of Large Water Clusters: Investigation Based on the Combination of the AMOEBA Potential and Generalized Energy-Based Fragmentation Approach. *J. Phys. Chem. A* **2010**, *114*, 9253−9261.

DOI: 10.1021/acs.jctc.6b00735
J. Chem. Theory Comput. 2017, 13, 55−76

(79) Raghavachari, K.; Trucks, G. W.; Pople, J. A.; Head-Gordon, M. A fifth-order perturbation comparison of electron correlation theories. *Chem. Phys. Lett.* **1989**, *157*, 479.
(80) Reed, A. E.; Curtiss, L. A.; Weinhold, F. Intermolecular Interactions From a Natural Bond Orbital, Donor-Acceptor Viewpoint. *Chem. Rev.* **1988**, *88*, 899−926.
(81) Weinhold, F.; Landis, C. R. *Valency and Bonding: A Natural Bond Orbital Donor-Acceptor Perspective*; Cambridge University Press: Cambridge, 2003.
(82) Lebedev, V. I.; Skorokhodov, L. Quadrature formulas of orders 41, 47 and 53 for the sphere. *Russian Acad. Sci. Dokl. Math.* **1992**, *45*, 587−592.
(83) Gräfenstein, J.; Cremer, D. Efficient DFT integrations by locally augmented radial grids. *J. Chem. Phys.* **2007**, *127*, 164113.
(84) Kazimirski, J.; Buch, V. Search for Low Energy Structures of Water Clusters $(H_2O)_n$, n = 20−22, 48, 123, and 293. *J. Phys. Chem. A* **2003**, *107*, 9762−9775.
(85) Bader, R. F. W. *Atoms in Molecules: A Quantum Theory*; Oxford University Press: Oxford, 1994.
(86) Cremer, D.; Kraka, E. A Description of the Chemical Bond in Terms of Local Properties of Electron Density and Ener. *Croat. Chem. A* **1984**, *57*, 1259−1281.
(87) Cremer, D.; Kraka, E. Chemical Bonds without Bonding Electron Density - Does the Difference Electron Density Analysis Suffice for a Description of the Chemical Bond? *Angew. Chem., Int. Ed. Engl.* **1984**, *23*, 627−628.
(88) Kraka, E.; Cremer, D. In *Theoretical Models of Chemical Bonding. The Concept of the Chemical Bond*; Maksic, Z. B., Ed.; Springer Verlag: Heidelberg, 1990; Vol 2, p 453.
(89) Zou, W.; Cremer, D. C_2 in a Box: Determining its Intrinsic Bond Strength for the $X^1\Sigma_g^+$ Ground State. *Chem. - Eur. J.* **2016**, *22*, 4087−4099.
(90) Wilson, E. B.; Decius, J. C.; Cross, P. C. *Molecular Vibrations. The Theory of Infrared and Raman Vibrational Spectra*; McGraw-Hill: New York, 1955.
(91) Zou, W.; Cremer, D. Properties of Local Vibrational Modes: The Infrared Intensity. *Theor. Chem. Acc.* **2014**, *133*, 1451.
(92) Decius, J. Compliance Matrix and Molecular Vibrations. *J. Chem. Phys.* **1963**, *38*, 241.
(93) Zou, W.; Kalescky, R.; Kraka, E.; Cremer, D. Relating Normal Vibrational Modes To Local Vibrational Modes Benzene and Naphthalene. *J. Chem. Phys.* **2012**, *137*, 084114.
(94) Hayward, R. J.; Henry, B. R. A General Local-Mode Theory for High Energy Polyatomic Overtone Spectra and Application to Dichloromethane. *J. Mol. Spectrosc.* **1975**, *57*, 221−235.
(95) Henry, B. R. The Local Mode Model and Overtone Spectra: A Probe of Molecular Structure and Conformation. *Acc. Chem. Res.* **1987**, *20*, 429−435.
(96) Rong, Z.; Henry, B. R.; Robinson, T. W.; Kjaergaard, H. G. Absolute Intensities of CH Stretching Overtones in Alkenes. *J. Phys. Chem. A* **2005**, *109*, 1033−1041.
(97) Kraka, E.; Larsson, J. A.; Cremer, D. In *Computational Spectroscopy: Methods, Experiments and Applications*; Grunenberg, J., Ed.; Wiley: New York, 2010; p 105.
(98) Badger, R. M. A Relation Between Internuclear Distances and Bond Force Constants. *J. Chem. Phys.* **1934**, *2*, 128−131.
(99) Kalescky, R.; Kraka, E.; Cremer, D. Identification of the Strongest Bonds in Chemistry. *J. Phys. Chem. A* **2013**, *117*, 8981−8995.
(100) Mahoney, M. W.; Jorgensen, W. L. A five-site model for liquid water and the reproduction of the density anomaly by rigid, nonpolarizable potential functions. *J. Chem. Phys.* **2000**, *112*, 8910−8922.
(101) Ewald, P. P. Die Berechnung optischer und elektrostatischer Gitterpotentiale. *Ann. Phys.* **1921**, *369*, 253−287.
(102) Uberuaga, B. P.; Anghel, M.; Voter, A. F. Synchronization of trajectories in canonical molecular-dynamics simulations: Observation, explanation, and exploitation. *J. Chem. Phys.* **2004**, *120*, 6363−6374.
(103) Berendsen, H. J. C.; Postma, J. P. M.; van Gunsteren, W. F.; DiNola, A.; Haak, J. R. Molecular dynamics with coupling to an external bath. *J. Chem. Phys.* **1984**, *81*, 3684−3690.
(104) Swope, W. C.; Andersen, H. C.; Berens, P. H.; Wilson, K. R. A computer simulation method for the calculation of equilibrium constants for the formation of physical clusters of molecules: Application to small water clusters. *J. Chem. Phys.* **1982**, *76*, 637−649.
(105) Ryckaert, J.-P.; Ciccotti, G.; Berendsen, H. J. Numerical integration of the cartesian equations of motion of a system with constraints: molecular dynamics of n-alkanes. *J. Comput. Phys.* **1977**, *23*, 327−341.
(106) Miyamoto, S.; Kollman, P. A. Settle: An analytical version of the SHAKE and RATTLE algorithm for rigid water models. *J. Comput. Chem.* **1992**, *13*, 952−962.
(107) Giguere, P. A. Bifurcated Hydrogen Bonds in Water. *J. Raman Spectrosc.* **1984**, *15*, 354−358.
(108) Tukey, J. W. *Exploratory Data Analysis*, 1st ed.; Addison Wesley: 1977.
(109) Kraka, E.; Zou, W.; Filatov, M.; Gräfenstein, J.; Izotov, D.; Gauss, J.; He, Y.; Wu, A.; Polo, V.; Olsson, L. et al. *COLOGNE16*; 2016.
(110) Frisch, M. J.; Trucks, G. W.; Schlegel, H. B.; Scuseria, G. E.; Robb, M. A.; Cheeseman, J. R.; Scalmani, G.; Barone, V.; Mennucci, B.; Petersson, G. A. et al. *Gaussian 09 Revision B.01*; Gaussian Inc.: Wallingford, CT, 2010.
(111) Case, D.; Berryman, J.; Betz, R.; Cerutti, D.; Cheatham, T., III; Darden, T.; Duke, R.; Giese, T.; Gohlke, H. et al. *AMBER 2015*; University of California: San Francisco, 2015.
(112) Lu, T.; Chen, F. Multiwfn: A Multifunctional Wavefunction Analyzer. *J. Comput. Chem.* **2012**, *33*, 580−592.
(113) Ohno, K.; Okimura, M.; Akai, N.; Katsumoto, Y. The effect of cooperative hydrogen bonding on the OH stretching-band shift for water clusters studied by matrix-isolation infrared spectroscopy and density functional theory. *Phys. Chem. Chem. Phys.* **2005**, *7*, 3005−3014.
(114) Iwata, S. Energy analysis of weak electron-donorĂ-acceptor complexes and water clusters with the perturbation theory based on the locally projected molecular orbitals: charge-transfer and dispersion terms. *Phys. Chem. Chem. Phys.* **2012**, *14*, 7787−7794.
(115) Iwata, S.; Bandyopadhyay, P.; Xantheas, S. S. Cooperative Roles of Charge Transfer and Dispersion Terms in Hydrogen-Bonded Networks of $(H_2O)_n$, n = 6, 11, and 16. *J. Phys. Chem. A* **2013**, *117*, 6641−6651.
(116) Wang, B.; Jiang, W.; Dai, X.; Gao, Y.; Wang, Z.; Zhang, R.-Q. Molecular orbital analysis of the hydrogen bonded water dimer. *Sci. Rep.* **2016**, *6*, 22099.
(117) Clark, T.; Politzer, P.; Murray, J. S. Correct electrostatic treatment of noncovalent interactions: the importance of polarization. *WIRES Comp. Mol. Sci.* **2015**, *5*, 169−177.
(118) Politzer, P.; Murray, J. S.; Clark, T. Mathematical modeling and Physical Reality in Non-covalent Interactions. *J. Mol. Model.* **2015**, *21*, 52−61.
(119) Politzer, P.; Murray, J. S.; Clark, T. σ-Hole Bonding: A Physical Interpretation. *Top. Curr. Chem.* **2014**, *358*, 19−42.
(120) Dominikowska, J.; Jablonski, M.; Palusiak, M. Feynman force components: basis for a solution of the covalent vs. ionic dilemma. *Phys. Chem. Chem. Phys.* **2016**, *18*, 25022−25026.
(121) Kraka, E.; Cremer, D. In *Theoretical Models of Chemical Bonding. The Concept of the Chemical Bond*; Maksic, Z., Ed.; Springer Verlag: Heidelberg, Germany, 1990; Vol 2, pp 453−542.
(122) Porterfield, W. W. *Inorganic Chemistry, A Unified Approach*; Academic Press: San Diego, 1993.
(123) Park, C.-Y.; Kim, Y.; Kim, Y. The multi-coefficient correlated quantum mechanical calculations for structures, energies, and harmonic frequencies of HF and H2O dimers. *J. Chem. Phys.* **2001**, *115*, 2926.
(124) Cherng, B.; Tao, F.-M. Formation of ammonium halide particles from pure ammonia and hydrogen halide gases: A theoretical

DOI: 10.1021/acs.jctc.6b00735
J. Chem. Theory Comput. 2017, 13, 55−76

study on small molecular clusters 2, 4; X = F, Cl, Br). *J. Chem. Phys.* **2001**, *114*, 1720.
(125) Steiner, T. The hydrogen bond in the solid state. *Angew. Chem., Int. Ed.* **2002**, *41*, 48.
(126) Nibbering, E.; Elsaesser, T. Ultrafast Vibrational Dynamics of Hydrogen Bonds in the Condensed Phase. *Chem. Rev.* **2004**, *104*, 1887.
(127) Diken, E.; Headrick, J.; Roscioli, J.; Bopp, J.; Johnson, M.; McCoy, A. Fundamental Excitations of the Shared Proton in the $H_3O_2^-$ and $H_5O_2^+$ Complexes. *J. Phys. Chem. A* **2005**, *109*, 1487.
(128) Diken, E.; Headrick, J.; Roscioli, J.; Bopp, J.; McCoy, A.; Huang, X.; Carter, S.; Bowman, J. Argon Predissociation Spectroscopy of the $OH^-{\cdot}H_2O$ and $Cl^- \cdot H_2O$ Complexes in the 1000−1900 cm^{-1} Region: Intramolecular Bending Transitions and the Search for the Shared-Proton Fundamental in the Hydroxide Monohydrate. *J. Phys. Chem. A* **2005**, *109*, 571.
(129) Brindle, C.; Chaban, G.; Gerber, R.; Janda, K. Anharmonic vibrational spectroscopy calculations for (NH_3) (HF) and (NH_3) (DF): fundamental, overtone, and combination transitions. *Phys. Chem. Chem. Phys.* **2005**, *7*, 945.
(130) Janeiro-Barral, P.; Mella, M. Study of the structure, energetics, and vibrational properties of small ammonia clusters $(NH_3)_n$ (n = 2−5) using correlated ab initio methods. *J. Phys. Chem. A* **2006**, *110*, 11244.
(131) Slipchenko, M.; Sartakov, B.; Vilesov, A.; Xantheas, S. Study of NH Stretching Vibrations in Small Ammonia Clusters by Infrared Spectroscopy in He Droplets and ab Initio Calculations. *J. Phys. Chem. A* **2007**, *111*, 7460.
(132) Elsaesser, T. Two-dimensional infrared spectroscopy of intermolecular hydrogen bonds in the condensed phase. *Acc. Chem. Res.* **2009**, *42*, 1220.
(133) Heisler, I.; Meech, S. Low-Frequency Modes of Aqueous Alkali Halide Solutions: Glimpsing the Hydrogen Bonding Vibration. *Science* **2010**, *327*, 857.
(134) Zhang, X.; Zeng, Y.; Li, X.; Meng, L.; Zheng, S. Comparison in the complexes of oxygen-containing sigma-electron donor with hydrogen halide and dihalogen molecules. *J. Mol. Struct.: THEOCHEM* **2010**, *950*, 27−35.
(135) Li, X.-Z.; Walker, B.; Michaelides, A. Quantum nature of the hydrogen bond. *Proc. Natl. Acad. Sci. U. S. A.* **2011**, *108*, 6369.
(136) de Lima, N.; Ramos, M. A theoretical study of the molecular structures and vibrational spectra of the $N_2O{\cdot}(HF)_2$. *J. Mol. Struct.* **2012**, *1008*, 29.
(137) Grabowski, S. Red- and Blue-Shifted Hydrogen Bonds: the Bent Rule from Quantum Theory of Atoms in Molecules Perspective. *J. Phys. Chem. A* **2011**, *115*, 12789.
(138) Mpemba, E.; Osborne, D. Cool. *Phys. Educ.* **1969**, *4*, 172−5.
(139) Huang, Y.; Zhang, X.; Ma, Z.; Zhou, Y.; Zheng, W.; Zhou, J.; Sun, C. Q. Hydrogen-bond relaxation dynamics: Resolving mysteries of water ice. *Coord. Chem. Rev.* **2015**, *285*, 109−165.

NOTE ADDED AFTER ASAP PUBLICATION

This paper was published ASAP on December 20, 2016 with errors in the text. The corrected version was reposted on December 21, 2016.

DOI: 10.1021/acs.jctc.6b00735
J. Chem. Theory Comput. 2017, 13, 55−76